DEVELOPMENT AND VALIDATION OF A UV-VIS BROADBAND CAVITY ENHANCED SPECTROMETER FOR AEROSOL EXTINCTION

by

JACLYN LECAROZ

(Under the Direction of Geoffrey Smith)

ABSTRACT

The radiative effects of atmospheric aerosols are the least constrained variable in many radiative forcing calculations. In an attempt to better quantify these particles many instrumental techniques have been developed to measure the optical properties of atmospheric aerosols. We have built a broadband cavity enhanced spectrometer for the measurement of aerosols in the UV-Vis spectral region. The instrument consists of three optical cavities that cover 385-425, 520-560, 630-685 nm. This large spectral coverage allows for accurate wavelength dependent aerosol extinction measurements. It is hoped that using measurements from this instrument can provide inputs to climate models that will aid in characterizing the direct effect. Such measurements include the extinction Ångström exponent, and the single scattering albedo when used in conjunction with our custom photoacoustic spectrometer.

INDEX WORDS: Cavity enhanced spectroscopy, Aerosols, Climate change, Radiative transfer, Extinction Ångström exponent

DEVELOPMENT AND VALIDATION OF A UV-VIS BROADBAND CAVITY ENHANCED SPECTROMETER FOR AEROSOL EXTINCTION

by

JACLYN LECAROZ

B.S., The University of Alabama, 2017

A Thesis Submitted to the Graduate Faculty of The University of Georgia in Partial Fulfillment of the Requirements for the Degree

MASTER OF SCIENCE

ATHENS, GEORGIA

2019

© 2019

Jaclyn Lecaroz

All Rights Reserved

DEVELOPMENT AND VALIDATION OF A BROADBAND CAVITY ENHANCED SPECTROMETER FOR AEROSOL EXTINCTION

by

JACLYN LECAROZ

Major Professor:	Geoffrey Smith
Committee:	Amanda Frossard
	Brandon Rotavera

Electronic Version Approved:

Ron Walcott
Interim Dean of the Graduate School
The University of Georgia
December 2019

DEDICATION

I'd like to dedicate this thesis to my sister, Samantha Lecaroz, although graduate school can be difficult at times, fighting for your health is a lot harder. Thank you for always offering perspective, advice, and inspiration to me throughout this journey.

ACKNOWLEDGEMENTS

This work is a result of a great deal of time and effort from numerous parties. First and foremost, I would like to thank Dr. Geoffrey Smith for all his professional support and guidance throughout my time here at The University of Georgia. This project and degree would not have been possible without his financial and personal support. I would also like to thank my fellow group members for not only being patient mentors to me, but also great friends. I would also like to thank numerous other faculty member at UGA for being guiding figures and also phenomenal teachers, Dr. Jeffrey Urbauer, Dr. Amanda Frossard, Dr. Richard Hubbard, and Dr. Ana West.

I would also like to thank my undergraduate professor, Dr. Michael Bowman, for building up my scientific confidence and molding me into a chemist. Finally, I'd like to thank my friends and family for their continuing support, encouragement, and love throughout this opportunity.

TABLE OF CONTENTS

Page

LIST OF TABLES

Page

LIST OF FIGURES

Page

CHAPTER 1

INTRODUCTION AND LITERATURE REVIEW

1.1 Atmospheric Chemistry and Aerosols in the Atmosphere

The study of atmospheric chemistry is crucial to the environment and human health, and although the field is relatively new compared to other areas of scientific study it is one of the most important in times of rapid climate change. Atmospheric chemistry includes the chemistry of the total of Earth's atmosphere.[1] This includes regions of relatively polluted areas, as well as relatively clean regions. Atmospheric chemistry is concerned with the whole of the atmosphere from the layers close to the Earth's surface to the upper atmosphere. The layers of the atmosphere each have their own distinct properties with changes in pressure and temperature common among layers of the atmosphere. There are many sources of particulate matter that affect our atmosphere, including both natural and anthropogenic sources.[2] John Evelyn in 17th century England even wrote about his concern of the London smog aerosols in his book, Fumifugium in 1661.[3] The parallels between the London smog in 1661 and the air quality concerns in modern day China are evident; this observation displays that the environmental and human health impacts of the atmosphere are an enduring dilemma.

The atmosphere affects the many different aspects of our world, including crop growth, human health, and the weather.[4] Temperature and solar radiation are both major variables in the growth of plants and these can both be affected greatly by changes in the atmosphere caused by aerosols or other pollutants. A change in global temperatures or solar radiation reaching the Earth's surface would change the relative climate of that area and also alter the amount of photosynthesis occurring within different plants.[5] Air pollution is also known to have various

effects on the health of humans. These effects can range from minor irritation of the upper respiratory system to more serious effects such as chronic bronchitis and lung cancer. It is also important to note that long term exposure to pollution has been linked to a reduced life expectancy in humans, so the study of these pollutants is essential.[6-7] Finally, it is well known that particulate matter, both anthropogenic and natural, can cause major effects on the global climate as well as regional weather. The warming of the Earth is primarily caused by greenhouse gases, however there are many other components that are not as well quantified that contribute to this major issue, including aerosol particles.[8]

An aerosol is defined as a collection of fine solid particles or liquid droplets suspended in either air or another gas.[9] Aerosols come in all shapes, sizes, and compositions. The general concentration of aerosols in the atmosphere are quantified in mass per volume. The lifetime of different aerosol particles in the atmosphere is important because the longer the lifetime of an aerosol the more of an overall potential impact it will have on the climate forcing within the atmosphere. Aerosols are classified in many different ways, one of these being particle diameter.[10] There are aerosol growth processes within the atmosphere that can change the diameter. For example, some aerosols are born from precursor gases such as H_2SO_4, NH_3 or other organic compounds released from emissions. These emissions include, but are not limited to, fossil fuel combustion, volcanic emissions, biomass burning, and other anthropogenic and natural sources.[1] These precursor gases undergo a process of nucleation, or the clustering of gas molecules to produce ultrafine aerosol particles approximately less than 0.01 μm in diameter. (Figure 1.1) These ultrafine aerosols condense and coagulate to form the larger accumulation aerosols that have a greater impact on climate forcing than the ultrafine particles. Understanding aerosol growth is vital to comprehending the lifetime of different aerosols within the atmosphere.[10]

Another aspect that is important to consider in understanding the lifetime of an aerosol particle is the deposition process. Generally, there are two main types of deposition, wet and dry. Dry deposition is more common for coarse aerosols as they are larger and settle to Earth's surface at a substantial rate, enough to be included as an additional removal rate.[11] There are methods used to quantify the dry deposition of different particles to account for this removal rate. The direct methods involve a sizeable amount of effort and complex instrumentation but have a low amount of assumptions to obtain an explicit measurement. The indirect methods are more derivation based, derived from secondary quantities like concentration gradients.[12] Wet deposition has a variety of forms, including precipitation scavenging, cloud interception, fog deposition, and snow deposition.[13] Precipitation scavenging occurs through the removal of aerosols by a raining cloud, whereas cloud interception is due to the impaction of cloud droplets onto terrain. Fog and snow deposition are the result of removal of species during settling fog droplets or during a snowstorm, respectively. Wet deposition is the main form of deposition for particulate matter in the atmosphere.[1] These deposition processes together are what decrease the concentrations of particulate matter in the atmosphere and significantly impact the lifetime of aerosol particles.

The reason why aerosols and their lifetime in the atmosphere is important is because of their effects on the climate. Aerosols can interact with Earth's energy budget both directly and indirectly.[13] The direct effect involves the phenomena of aerosols both scattering and absorbing incoming solar radiation within the atmosphere and how this interaction affects Earth's radiative balance. The indirect effect includes the ability of aerosols to act as surfaces for water droplets to condense on and to act as cloud condensation nuclei.[14] This indirect effect is important because clouds interact with solar radiation in the atmosphere. Different kinds and sizes of aerosols can affect clouds differently, and thus have different indirect effects on the energy balance of the

Earth. For example, a cloud that is forming in a more polluted area will distribute the water droplets over a larger number of aerosol particles causing a larger cross section of cloud droplets and thus a larger cloud albedo.[13] (Figure 1.2) This albedo directly affects global radiative budget by increasing the respective albedo of Earth as well. The argument could be made that this effect of aerosols is assisting in buffering the effects of global warming caused by greenhouse gases because of this indirect effect raising Earth's albedo and enhancing cooling. However, there are many variables to take into account in order to quantify the total overall effect that aerosols have on the radiative budget.[14]

In many computer climate models, predicting the radiative forcing of pollutants and gases in the atmosphere the largest uncertainties are shown as the aerosols in the atmosphere. (Figure 1.3) The Intergovernmental Panel on Climate Change (IPCC) estimates that the direct radiative forcing globally of aerosols as a whole is $-0.50 \pm 0.40 \frac{W}{m^2}$.[13] The large error bar is as a result of the many unknowns in quantifying the effects of aerosols. Some of these difficulties are as a result of the short lifetime of aerosols. The concentrations of aerosols are highly variable inter-day and are also stochastic interregionally. An important reason as to why the radiative forcing is so uncertain, is the fact that some particles absorb and some scatter light, which can lead to them competing in the radiative forcing and can cause aerosols in different areas have a different regional effect than in other areas. Along with varying concentrations, less studied particles, such as organic aerosols, are largely contributing to the uncertainty through the direct effect.[15] The direct effect can be harder to quantify than other atmospheric components because of varying particle composition and size. This large uncertainty in the effect of aerosols on the radiative budget is a large part in why aerosols need to be heavily studied in the field of atmospheric chemistry.

Overall, there are many uncertainties in the radiative forcing calculation and thus there are large errors in climate models when these effects are used in them. Climate models simulate the behavior of different climate forcings in order to create projections of future climate behavior. The climate models are used to predict global temperatures, weather patterns, and precipitation. The atmospheric component of these models include the different gas composition of the air at different layers as well as the particulate matter within the atmosphere. The effects from aerosols are essential to evaluating the effectiveness of climate models in general. The hope is that these climate models will be able to predict future changes in carbon dioxide emissions and aerosol effects in the climate radiative forcing reliably.[16] Therefore, the error bars that are present currently on the radiative forcing measurement cause a great deal of problems.[17] The changing concentrations of aerosols regionally and the different optical effects of different aerosols greatly contribute to these large error bars, making the optical effects of ambient aerosols an important area of atmospheric chemistry to explore.

1.2 Optical Properties of Aerosols

Optical properties of atmospheric aerosols are a way of describing the interactions of a variety of particulate matter with light, or incoming solar radiation as it pertains to the atmosphere. These interactions can be simplified into scattering and absorption. Scattering is defined as a change in the direction of propagation of a radiation beam caused by a particle in its path without absorbing any of this radiation.[10] There are many different types of scattering such as reflection, refraction, diffraction, or a combination of these effects. This scattering effect is known to have a net cooling effect on the global radiative budget, because the incoming solar radiation is reflected back into space by these scattering particles therefore decreasing the amount of light absorbed by the Earth.[13] Particles on the same order of magnitude as the wavelength of light are some of the most efficient scatterers and cause a large cooling effect for

their size.[1] On the other hand, absorption is the interaction of the radiation beam being transformed by the particle from light energy into thermal energy. As a result of this interaction the thermal energy in released and causes heating of the lower atmosphere. However, the light that is absorbed is no longer able to reach Earth's surface so this could also contribute to localized cooling.[10] This phenomenon was observed by the aerosols of volcanic ash in Pinatubo when the global temperature dropped as a result of a major eruption which caused a large concentration of aerosols to block incoming light.[18] Although this cooling effect is present, the net effect of absorption is warming because atmospheric circulation and mixing processes redistribute this thermal energy.[10] The sum of the light scattering and absorbing properties of an aerosol is referred to as aerosol extinction.[19] The extinction is the total of the overall effect of the aerosol. Therefore, the extinction can give useful information on how each aerosol can contribute to the radiative budget.[20]

One of the factors that affects these optical properties is the refractive index of the particle. The refractive index is defined as a description of the innate property of how light is propagated through a substance. This complex refractive index has a real phase velocity component and an imaginary attenuation component.[21] (Equation 1.1) This intrinsic property is described by the equation

$$m = n + ik \tag{1.1}$$

where m is the complex refractive index and n corresponds to the "real" scattering component of the refractive index, and the k refers to the "imaginary" absorption factor. The refractive index is key to understanding the direct effect that aerosols have on the radiative budget.[10] This is a large unknown in the quantification of aerosol effects on the radiative budget for climate models.

The fact that the absorption and scattering components account for the total light extinction mirrors the fact that the sum of the absorption cross section and scattering cross

section equals the extinction cross section. (Equation 1.2) The extinction cross section is the probability that a photon of light will interact with the particle, because it sums both of the light interactions. These optical properties are referred to in terms of cross sections because the cross section has units of area.[22] This interaction can be either absorption or scattering, and each can be divided up into its own subparts. This is shown by the relationship

$$\sigma_{ext} = \sigma_{abs} + \sigma_{scat} \tag{1.2}$$

where σ_{abs} is the absorption cross section and σ_{scat} is the scattering cross section.[23] This sum of the cross sections is key to understanding the overall optical direct effect of aerosols. These experimental and theoretically derived values allow us to find the different coefficients that show the effect that these aerosols have on the climate.

One of the theoretical approaches to quantifying these effects of the aerosols is named Generalized Lorenz-Mie Theory (GLMT) which is a complex theory for scattering by perfect spheres. This theory takes into account the incident beam, the scattered beam, and the light inside the sphere. GLMT can be used to obtain the scattering, absorption, and extinction cross sections. GLMT describes the regime where wavelength and particle diameters are comparable in size, and the theory is used to predict the scattering and absorption portions of the extinction.[24] However, most aerosols are not perfect spheres[25] and not perfectly homogenous so very often, experimentally retrieved data does not perfectly match with the predicted result from Mie theory.

Another large unknown in the study of atmospheric aerosols is the composition of ambient aerosols. There are many ambient aerosols that are not as easily quantified as purely scattering such as ammonium sulfate. An example of these aerosols is light absorbing organic matter also known as brown carbon.[26] These are carbon-based particles created from sources such as biomass burning or incomplete combustion.[27] There are many factors about organic carbon in the atmosphere that are not well quantified. For example, the composition of the

particle does not solely predict the optical properties of the particle. These particles do not tend to be perfectly spherical or homogeneous making them much harder to model than other aerosols. Organic aerosols make up a large part of ambient aerosols in many regions, and because of the difficulties in quantifying the optical effects there is a need for an improved measurement of their effects on the radiative budget.[14]

1.3 Measurement of Aerosol Optical Properties

Quantitative measurements of atmospheric aerosols offer many challenges. For one, the aerosol concentrations in different locations are highly variable at a singular location let alone in a different region entirely. This causes measurements to be limited to certain locations especially since not every quantitative measurement technique is mobile and able to sample in field measurements. It is difficult to find a technique that is both sensitive and accurate, especially for aerosol optical properties. The measurement technique must be effective over a wide range of concentrations in order to span the ambient conditions that are present.[14] Optimally a real time measurement is done to view the small and large changes that can occur in ambient measurements. In order to quantify the optical effect of different aerosols discrepancies between instruments and techniques must be justified and even still, if the relative uncertainties of instruments are larger than the measurement derived the data is not usable. An example of this is the subtraction method where the scattering and extinction of a particle are measured and the absorbance is found from the difference between these two measurements. This type of technique is effective in certain scenarios, however it is usually not ideal for only marginally absorbing aerosols.

In the past, absorption and scattering have been measured separately using both in-situ and filter-based methods,[28] such as photoacoustic spectrometry, polar nephelometry, particle soot

absorption photometry, aethalometry, and others.[29,30] Customarily, two or more of these instruments would be used together to determine the total aerosol extinction. Filter based methods involve the collection of particles over time onto a filter which is then compared to a blank filter or measured optically in solution rather than in suspended aerosol. The flow rate of the sample flow can be used to find the approximate concentration of the sampled particles.[31] Morphology and changes in composition among particles would affect the effectiveness of these methods and thus, this method is not as precise, which may not be ideal for optical aerosol measurements. Although these techniques are available at multiple wavelengths, due to artifacts present in filter-based methods, it is probable to suggest that these methods alone may not be able to produce true extinction measurements.[28] In-situ measurements offer a less invasive method` to measure optical properties directly or indirectly. The in-situ technique is therefore favored by many different instruments that measure aerosol optical properties.[29]

An in-situ technique that measures the light absorption of an aerosol directly is the photoacoustic spectrometer, or PAS.[32] Photoacoustic spectroscopy uses modulated lasers to have particles be exposed to light of a specific wavelength. These particles absorb this light energy and this causes local heating, this temperature change creates a pressure or sound wave. The specific frequency of the laser beam and the resultant sound waves are detected by a highly sensitive microphone within photoacoustic cavity. This technique provides a highly sensitive way to detect the absorption of aerosols in a very short amount of time. Detection limits can be less than 1 Mm^{-1} for a 60 second measurement.[33] The absorbing species can be quantified using this technique, however the scattering is not able to be retrieved during this process. This can cause some issues because of the sheer amount of scattering particles in the atmosphere, and the extinction often shows that ambient aerosols are dominated by scattering properties. However,

without direct absorption methods, finding the absorption coefficient would have large errors with such a small amount of absorption.

Another in situ spectroscopy technique for measuring the total extinction of aerosol particles is called Cavity Ring-Down Spectroscopy or CRDS.[34, 35] This technique has two highly reflective dielectric mirrors on either end of a cavity where light is injected and slowly transmitted through one of the mirrors. The time that a photon can survive in the cavity is known as the ring down time. This technique is highly sensitive to losses in the form of particles interacting with light instead of mirrors, and because of this sensitivity, CRDS has a variety of uses, but for this project extinction applications will be the focus.[36, 37] CRDS uses a laser at a specific wavelength to inject into the cavity so that all extinction detected by a detector is at a known wavelength. Multiple of these wavelengths can be put together to derive an extinction coefficient for each sample. A steady sample flow of laboratory aerosols or ambient aerosols are flowed through a CRD cell, and when concentration, morphology, and size distribution are known it is possible to derive a CRI by comparing to Mie theory.

An alternative in-situ approach, broadband cavity enhanced spectroscopy (BBCES) has obtained recognition as a means to measure total extinction. Similar to CRDS, BBCES allows for the monitoring of trace gases to remove fluctuations from background to background when performing experiments resulting in more accurate experimentation, while also having a broader spectral coverage because of the selected light source. BBCES consists of a broadband light source collimated by a lens into an optical cavity that consists of two highly reflective dielectric mirrors. The integrated intensity of light transferred through the back mirror is sent to a detector such as a spectrophotometer. The broadband light source, for example an LED, allows BBCES to not be limited to a single wavelength which allows for a large advantage from single

wavelength CRDS. The larger spectral coverage also allows for extinction exponents to be derived from these points.[38, 39]

When combined, a broadband cavity enhanced spectrometer, with a large spectral coverage, and a PAS, with multiple wavelengths, can be used to determine many optical properties of aerosols. The PAS having the smaller part of the CRI allows for less error to be found in the difference method in order to find the scattering. Subtracting a small number (absorption) from a large number (extinction) to retrieve another large number (scattering) allows for much lower uncertainty than if absorption was not quantified. Both of these techniques are in-situ and allow for rapid results. The low detection limits make this pair an ideal candidate for sampling ambient aerosols. These two technologies together can retrieve important quantities such as SSA, CRI, Extinction angstrom exponent (EAE), and absorption angstrom exponent (AAE). These intrinsic characteristics of aerosols particles are crucial to determining their effect on Earth's radiative budget, so having instruments to find these properties of ambient aerosols are imperative if we are to create better climate predicting models.[14, 31]

1.4 Goals of this work

Although there are many techniques and different forms of instrumentation to measure ambient aerosols, their effect on climate and the radiative budget still has a large uncertainty.[13] In order to improve this uncertainty, there is a need for better optical property measurements. This includes the extinction of aerosol particles. At the start of this project the goal was to develop a broadband cavity enhanced spectrometer and trouble shoot various errors in extinction measurements using laboratory generated particles that have a well-studied extinction cross section and refractive index. The fast-moving pace of this project has allowed this project to develop into a validation of this laboratory constructed three channel broadband cavity enhanced

spectrometer. We hope to show that this three-channel broadband cavity enhanced spectrometer with large wavelength coverage will improve the state of the art in measuring aerosol optical properties. The instrument accuracy and large spectral coverage would aid in quantifying optical effects of aerosols and improving climate models.

Chapter 1 Figures

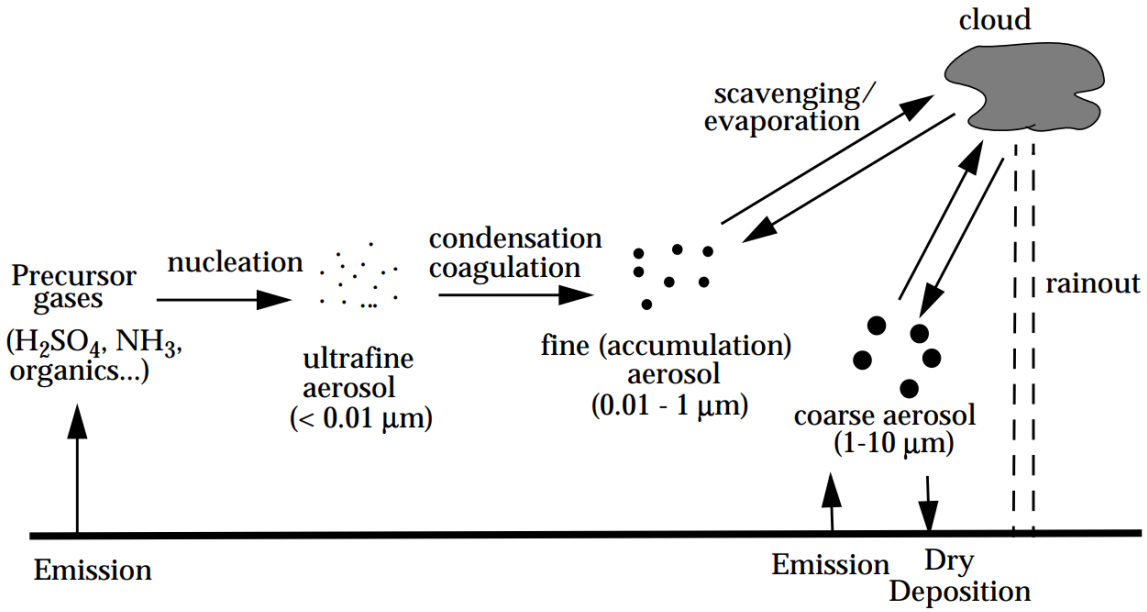

Figure 1.1 Potential Life Cycles of Aerosols
Introduction to Atmospheric Chemistry figure showing the production, growth and removal of atmospheric aerosols. Reproduced in full Jacobs 1999.[10]

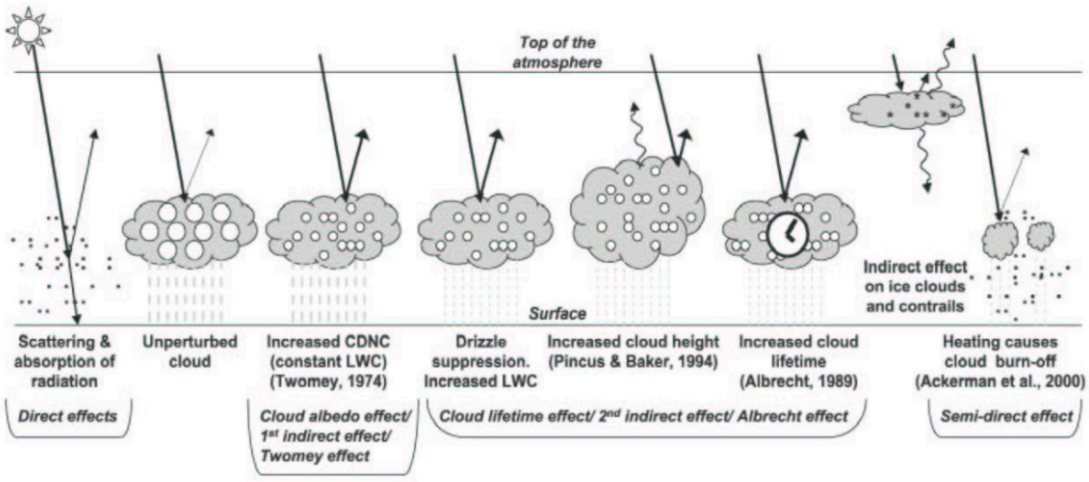

Figure 1.2 Aerosol and Light Interactions
IPCC figure showing different interactions of incident light, in this case solar radiation, and aerosols that can have an influence on the radiative energy budget. Reproduced in full IPCC 2013.[13]

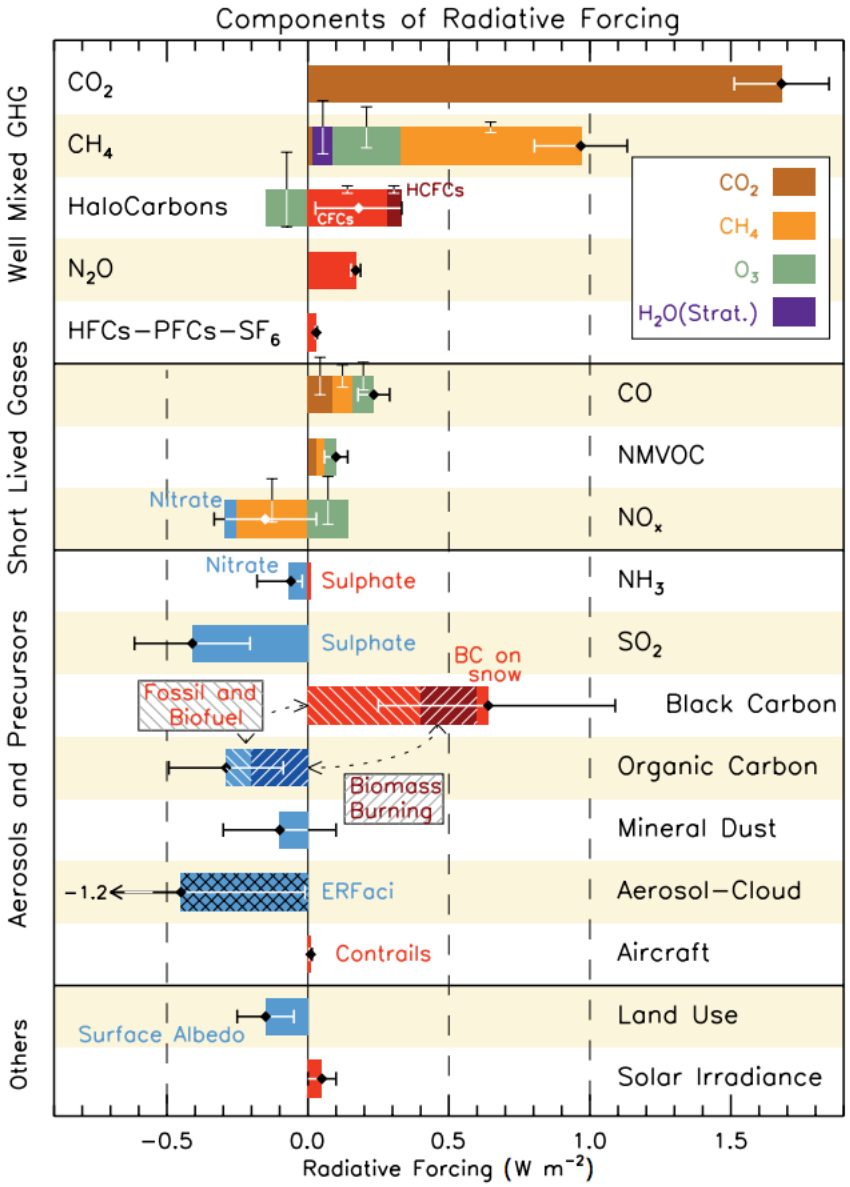

Figure 1.3 Components of Radiative Forcing
Intergovernmental Panel on Climate Change figure showing net radiative forcings of different components in the atmosphere including gases and aerosols. Reproduced in full IPCC 2013.[13]

References

1. Finlayson-Pitts, B.; Pitts, J. *Chemistry of the Upper and Lower Atmosphere*; Academic Press: London, UK, 2000.
2. Brimblecombe, P. Air Pollution in Industrializing England. *J. Air Pollut. Control Assoc.* **2012**, *28* (2), 115–118. https://doi.org/10.1080/00022470.1978.10470577.
3. Evelyn, J. *Fumifugium*; His Majesties Command: London, UK, 1661.
4. Greenwald, R.; Bergin, M. H.; Xu, J.; Cohan, D.; Hoogenboom, G.; Chameides, W. L. The Influence of Aerosols on Crop Production: A Study Using the CERES Crop Model. *Agric. Syst.* **2006**, *89* (2–3), 390–413. https://doi.org/10.1016/J.AGSY.2005.10.004.
5. Lelieveld, J.; Posch, U. *Chemists Can Help to Solve the Air-Pollution Health Crisis*; 2017.
6. Kampa, M.; Castanas, E. Human Health Effects of Air Pollution. *Environ. Pollut.* **2008**, *151*. https://doi.org/10.1016/j.envpol.2007.06.012.
7. Ghorani-Azam, A.; Riahi-Zanjani, B.; Balali-Mood, M. Effects of Air Pollution on Human Health and Practical Measures for Prevention in Iran. *J. Res. Med. Sci.* **2016**, *21*, 65. https://doi.org/10.4103/1735-1995.189646.
8. Oreskes, N. The Scientific Consensus on Climate Change. *Science.* **2004**, *306* (5702), 1686–1686. https://doi.org/10.1126/science.1103618.
9. Hinds, W. C. *Aerosol Technology Properties, Behavior, and Measurement OfAirborne Particles Second Edition*; Wiley-Interscience Publication, 1999.
10. Jacob, D. J. *Introduction to Atmospheric Chemistry*; Princeton University Press, 1999.
11. Seinfeld, J. H.; Pandis, S. N. *Atmospheric Chemistry and Physics : From Air Pollution to Climate Change*.

12. Pacyna, J. M. Atmospheric Deposition. *Encycl. Ecol.* **2008**, 275–285. https://doi.org/10.1016/B978-008045405-4.00258-5.

13. IPCC, 2013: *Climate Change 2013: The Physical Science Basis. Contribution of Working Group I to the Fifth Assessment Report of the Intergovernmental Panel on Climate Change* [Stocker, T. F., D. Qin, G. K. Plattner, M. Tignor, S.K. Allen, J. Boschung, A. Nauels, Y. Xia, V. Bex and P. M. Midgley (eds.)]. Cambridge University Press, Cambridge, United Kingdom and New York, NY, USA, 1535 pp, doi:10.1017/CBO9781107415324.

14. Trenberth, K. E.; Fasullo, J. T.; Kiehl, J. Earth's Global Energy Budget. *Bull. Am. Meteorol. Soc.* **2009**, *90* (3), 311–324. https://doi.org/10.1175/2008BAMS2634.1.

15. Penner, J. E.; Andreae, M.; Annegarn, H.; Barrie, L.; Feichter, J.; Hegg, D.; Jayaraman, A.; Leaitch, R.; Murphy, D.; Nganga, J.; et al. *Aerosols, Their Direct and Indirect Effects*.

16. Charlson, R. J.; Schwartz, S. E.; Hales, J. M.; Cess, R. D.; Coakley, Jr., J. A.; Hansen, J. E.; Hofmann, D. J. Climate Forcing by Anthropogenic Aerosols. *JSTOR* **1992**, *255*, 423–431.

17. Ghan, S.; Penner, J. E. ARM-Led Improvements in Aerosols in Climate and Climate Models. *Am. Meteorol. Soc.* **2016**, *57*. https://doi.org/10.1175/AMSMONOGRAPHS-D-15-0033.1.

18. McCormick, M. P.; Thomason, L. W.; Trepte, C. R. Atmospheric Effects of the Mt Pinatubo Eruption. *Nature* **1995**, *373* (6513), 399–404. https://doi.org/10.1038/373399a0.

19. Schuster, G. L.; Dubovik, O.; Holben, B. N. Angstrom Exponent and Bimodal Aerosol Size Distributions. *J. Geophys. Res.* **2006**, *111* (D7), D07207. https://doi.org/10.1029/2005JD006328.

20. Russell, P. B.; Bergstrom, R. W.; Shinozuka, Y.; Clarke, A. D.; DeCarlo, P. F.; Jimenez, J. L.; Livingston, J. M.; Redemann, J.; Dubovik, O.; Strawa, A. Absorption Angstrom Exponent in AERONET and Related Data as an Indicator of Aerosol Composition. *Atmos. Chem. Phys.* **2010**, *10* (3), 1155–1169. https://doi.org/10.5194/acp-10-1155-2010.

21. Mathai, C. V.; Harrison, A. W. Estimation of Atmospheric Aerosol Refractive Index. *Atmos. Environ.* **1980**, *14* (10), 1131–1135. https://doi.org/10.1016/0004-6981(80)90177-8.

22. Cotterell, M. I.; Mason, B. J.; Preston, T. C.; Orr-Ewing, A. J.; Reid, J. P. Optical Extinction Efficiency Measurements on Fine and Accumulation Mode Aerosol Using Single Particle Cavity Ring-down Spectroscopy. *Phys. Chem. Chem. Phys.* **2015**, *17* (24), 15843–15856. https://doi.org/10.1039/C5CP00252D.

23. Plass, G. N. Mie Scattering and Absorption Cross Sections for Absorbing Particles. *Appl. Opt.* **1966**.

24. Lock, J. A.; Rard Gouesbet, G. Generalized Lorenz-Mie Theory and Applications. *J. Quant. Spectrosc. Radiat. Transf. 110*, 800–807. https://doi.org/10.1016/j.jqsrt.2008.11.013.

25. Toon, O. B.; Pollack, J. B. A Global Average Model of Atmospheric Aerosols for Radiative Transfer Calculations. *Journal of Applied Meteorology (1962-1982)*. American Meteorological Society 1976, pp 225–246. https://doi.org/10.2307/26177372.

26. Saleh, R.; Cheng, Z.; Atwi, K. The Brown–Black Continuum of Light-Absorbing Combustion Aerosols. *Environ. Sci. Technol. Lett.* **2018**, *5* (8), 508–513. https://doi.org/10.1021/acs.estlett.8b00305.

27. Feng, Y.; Ramanathan, V.; Kotamarthi, V. R.; Kotamarthi, V. Brown Carbon: A Significant Atmospheric Absorber of Solar Radiation? *Atmos. Chem. Phys.* **2013**, *13* (17), 8607–8621. https://doi.org/10.5194/acp-13-8607-2013.

28. Lim, S.; Lee, M.; Kim, S. W.; Yoon, S. C.; Lee, G.; Lee, Y. J. Absorption and Scattering Properties of Organic Carbon versus Sulfate Dominant Aerosols at Gosan Climate Observatory in Northeast Asia. *Atmos. Chem. Phys.* **2014**, *14* (15), 7781–7793. https://doi.org/10.5194/acp-14-7781-2014.

29. Fuchs, H.; Dube, W. P.; Lerner, B. M.; Wagener, N. L.; Williams, E. J.; Brown, S. S. A Sensitive and Versatile Detector for Atmospheric NO 2 and NO X Based on Blue Diode Laser Cavity Ring-Down Spectroscopy. *Rev. Sci. Instrum* **2008**, *79*. https://doi.org/10.1021/es902067h.

30. Galleani, L.; Tavella, P. The Dynamic Allan Variance. *IEEE Trans. Ultrason. Ferroelectr. Freq. Control* **2009**, *56* (3), 450–464. https://doi.org/10.1109/TUFFC.2009.1064.

31. Jacobson, M. Z. Global Direct Radiative Forcing Due to Multicomponent Anthropogenic and Natural Aerosols. *J. Geophys. Res. Atmos.* **2004**, *106* (D2), 1551–1568. https://doi.org/10.1029/2000jd900514.

32. Mogo, S.; Cachorro, V. E.; Lopez, J. F.; Montilla, E.; Torres, B.; Rodríguez, E.; Bennouna, Y.; de Frutos, A. M. In Situ Measurements of Aerosol Optical Properties and Number Size Distributions in a Coastal Region of Norway during the Summer of 2008. *Atmos. Chem. Phys.* **2012**, *12* (13), 5841–5857. https://doi.org/10.5194/acp-12-5841-2012.

33. McClelland, J. F. Photoacoustic Spectroscopy. *Anal. Chem.* **1983**, *55* (1), 89–105. https://doi.org/10.1021/ac00252a003.

34. Fischer, D. Al; Smith, G. D. A Portable, Four-Wavelength, Single-Cell Photoacoustic Spectrometer for Ambient Aerosol Absorption. *Aerosol Sci. Technol.* **2018**, *52* (4), 393–406. https://doi.org/10.1080/02786826.2017.1413231.

35. Ramanathan, V.; Chung, C.; Kim, D.; Bettge, T.; Buja, L.; Kiehl, J. T.; Washington, W. M.; Fu, Q.; Sikka, D. R.; Wild, M. *Atmospheric Brown Clouds: Impacts on South Asian Climate and Hydrological Cycle*; 2005.

36. Ackerman, A. S.; Toon, O. B.; Taylor, J. P.; Johnson, D. W.; Hobbs, P. V; Ferek, R. J. Effects of Aerosols on Cloud Albedo: Evaluation of Twomey's Parameterization of Cloud Susceptibility Using Measurements of Ship Tracks. *J. Atmos. Sci.* **2000**, *57* (16), 2684–2695.

37. Twomey, S. *Pollution and the Planetary Albedo*; Pergamon Press, 1974.

38. Alexander, D.; Crozier, P. A.; Anderson, J. R. Brown Carbon Spheres in East Asian Outflow and Their Optical Properties. *Science (80-.).* **2008**, *321*, 833–836. https://doi.org/10.1126/science.1155296.

39. Washenfelder, R. A.; Flores, J. M.; Brock, C. A.; Brown, S. S.; Rudich, Y. Broadband Measurements of Aerosol Extinction in the Ultraviolet Spectral Region. *Atmos. Meas. Tech* **2013**, *6*, 861–877. https://doi.org/10.5194/amt-6-861-2013.

40. Zhao, W.; Dong, M.; Chen, W.; Gu, X.; Hu, C.; Gao, X.; Huang, W.; Zhang, W. Wavelength-Resolved Optical Extinction Measurements of Aerosols Using Borad-Band Cavity-Enhanced Absorption Spectroscopy over the Spectral Range of 445-480 Nm. *Anal. Chem* **2013**, *85*, 43. https://doi.org/10.1021/ac303174n.

CHAPTER 2

A 3- CHANNEL BROADBAND CAVITY ENHANCED SPECTROMETER FOR MEASURING UV-VIS AEROSOL EXTINCTION

[1]Lecaroz, J. and M. Pogash, D. A. Fischer, G. Smith. To be submitted to *Aerosol Science and Technology.*

Abstract

Here we describe a broadband cavity enhanced spectrometer (BBCES-III) designed to measure extinction by atmospheric aerosols throughout the UV-Visible spectrum. The instrument consists of three optical cavities that cover 385- 425, 520-560, 630-685 nm. Each cavity is illuminated by individual light-emitting diodes, and transmitted light is collected and transferred via a fiber optic cable to a spectrophotometer. With mirror reflectivity values above 99.98 %, effective pathlengths up to 3.15 km are achieved with the 0.25 m cavity. The detection limit of the instrument is better than 1.5 Mm^{-1} with a 1-minute integration time for all wavelengths allowing measurement of ambient aerosol extinction under most loading conditions. The instrument accuracy is validated with measurements of Rayleigh scattering by gases (argon, oxygen, carbon dioxide), absorption by a gas (NO_2), and extinction by both purely scattering and strongly absorbing laboratory-generated aerosols (Cargille Index Matching Fluid, Nigrosin). For 15 hours, the BBCES-III sampled atmospheric aerosols in tandem with a photoacoustic spectrometer (MultiPAS-IV) (406, 532, 662, 780 nm) and two cavity ringdown spectrometers (CRD) (445, 662 nm). The correlation between the 445 and 662 nm CRD and BBCES-III extinction measurements gave slopes of 1.04 and 0.97 and R^2 of 0.91(445 nm) and 0.97(662 nm). Using the BBCES-III and MultiPAS-IV measurements, the Single Scattering Albedo (SSA) and the Extinction Ångström Exponent (EAE) were measured and are reported.

2.1 Introduction

The effects of atmospheric aerosols on climate are not well quantified.[1,2] Atmospheric aerosols interact with solar radiation directly through absorption and scattering, and indirectly by altering the lifetime and albedo of clouds.[1] The direct interaction between an aerosol particle and incident radiation is determined by the wavelength of radiation and physiochemical properties of

the particle, including the size, shape, and complex refractive index.[3,4] Atmospheric aerosols are emitted by numerous sources and the optical properties of different aerosols can cause various effects on the total energy budget.[1,5] For example, some particles, such as ammonium sulfate, only scatter and do not absorb light, thereby reflecting solar energy leading to a cooling effect on the atmosphere.[5] On the other hand, absorbing particles, such as black carbon, can have a warming effect.[6] It is also believed that aerosols partially offset the large, warming effect of greenhouse gases, but the magnitude of the effect is poorly quantified.[1] It is crucial to understand better than direct effects of atmospheric aerosols in order to assist predictive global climate models.[1] Additionally, better constraints on aerosol optical properties improve the precision of satellite-retrievals.[2]

To improve the understanding of aerosol direct effects, wavelength resolved aerosol optical properties are needed.[7] One such property is aerosol extinction, which is the sum of the scattering and absorption. The extinction spectrum from ambient atmospheric aerosols often follows a power law functional form, typically defined as, $\propto (\lambda) = B\lambda^{-EAE}$,where B is a scaling factor and EAE is the extinction Ångström exponent,[8] which characterizes the wavelength dependence of the spectrum. In the past, absorption and scattering have been measured separately using both in situ and filter-based methods, such as photoacoustic spectrometry, polar nephelometry, particle soot absorption photometry, aethalometry, and others.[9-11] Customarily, two or more of these instruments would be combined to determine the total aerosol extinction. However, due to artifacts present in filter-based methods and the limited wavelengths available with laser-based instruments, it is probable to suggest that alternative methods with larger wavelength coverage may be able to produce improved extinction spectra. Direct measurements of extinction are also possible using long path instruments, however measurements of ambient

aerosols have not been displayed by such instruments, possibly due to the large limits of detection (LOD).[12, 13]

An alternative approach, broadband cavity enhanced spectroscopy (BBCES) can measure total extinction with larger spectral coverage than other techniques.[3, 11, 14-18] BBCES consists of a broadband light source collimated by a lens into an optical cavity that consists of two highly reflective mirrors. The integrated intensity of light transferred through the back mirror is sent to a photodetector such as a spectrophotometer. The broadband light source, often an LED or lamp, allows BBCES to have broad wavelength coverage, which may be advantageous over cavity ring down spectroscopy.[3, 15]

BBCES is a relatively new method, with the first demonstration of a broadband cavity enhanced spectrometer in 1996.[19] Consequently, there are few broadband cavity-enhanced spectrometers with expansive wavelength coverage. Recent reviews have discussed the state of this technique. Gas phase measurements have been reviewed by Zheng et al.,[18] and aerosol measurements have been reviewed by He et al.[11] Up until this point, only one BBCES has been developed with full visible spectral coverage (400-650 nm). The instrument uses custom coated mirrors to create large spectral coverage and a Xenon light source.[11]

Here, we present a portable, broadband cavity-enhanced spectrometer featuring three optical cavities that yield extinction measurements at 385-425, 520-560, and 630-685 nm. Although this is not continuous wavelength coverage, extinction can easily be interpolated between these regions by fitting to a power law. The instrument was developed to be mobile and features a relatively small cavity length of 25 cm. In this work, we present measurements validating the accuracy of the BBCES-III, including the Rayleigh scattering by gases (Ar, O_2, and CO_2), the absorption cross section of a strongly absorbing atmospheric pollutant (NO_2), and laboratory-generated aerosols, Nigrosin (Sigma Aldrich, CAS# 8005-03-6) and Cargille Index

Matching Fluid (Cargille Laboratories, L-CABK-1181). Furthermore, the instrument was operated in tandem with a photoacoustic spectrometer, MultiPAS-IV, and two cavity ringdown spectrometers (CRDS) to measure ambient atmospheric aerosols at Athens, GA [33.9485° 83.3740°].[20] The Extinction Ångström Exponent was derived from the BBCES-III and validated with CRD. The MultiPAS-IV yields absorption measurements at 406, 532, 662, and 780 nm, while the two CRD have wavelengths of 445 and 662 nm. The combination of the MultiPAS-IV and BBCES-III allowed measurement of the Single-Scattering Albedo (SSA). This work provides an alternative method for measuring ambient atmospheric aerosol extinction with large spectral coverage. The modular and relatively inexpensive design provides a platform for the development of other broadband cavity-enhanced spectrometers of any desired wavelengths.

2.2 Experimental

A three-channel, incoherent broadband cavity enhanced spectrometer has been developed to measure aerosol extinction from 385- 425, 520-560, and 630-685 nm. The instrument is dubbed the BBCES-III, and a schematic is presented in Figure 2.1. Instrument control and data acquisition is automated by custom software written in LABVIEW. This instrument is ultimately intended for field measurements; therefore, the BBCES-III was designed to be on a small, portable platform. The BBCES-III is mounted on a breadboard with dimensions of 50.8 x 30.5 cm, has a weight of 10 kg, and a total power consumption of 70 W.

2.2.1 Instrument Description

The BBCES-III features 3 channels. In each channel, a 25.4 mm f/1 plano-convex lens (Thorlabs, Inc.) collimates the output of an LED. The light is directed into an optical cavity formed by a set of one-inch diameter mirrors (Aerodyne) with a radius of curvature of 0.25 m

and a reflectivity greater than 99.97% for all wavelengths reported. The mirrors are separated by a distance of 0.252 m, closely matching the mirror radius of curvature, to create a nearly conformal cavity with optimal intensity throughput.[21] The transmitted light of each channel is optically filtered and focused using an optical filter listed in Table 1 and a 25 mm f/1 1.25 aspheric condenser lens (Thorlabs, Inc.) onto a SMA collector and transferred via a quadfurcated fiber optic cable to a single grating spectrophotometer with CCD array detector (Ocean Optics QE65000). The wavelength scale of the spectrophotometer was calibrated according to the user manual using emission lines from a Hg pen lamp (UVP, LLC). Furthermore, the wavelength calibration was validated using the extinction cross section of NO_2, and slight variations (<0.15 nm) in the wavelength calibration were corrected to the NO_2 cross section of Burrows et al.[22] The spectrophotometer observes wavelengths from 200-975 nm with a resolution greater than 0.8 nm. An integration time of 100 ms gives an appropriate photon count on the CCD at each wavelength and is used for all measurements. Typically, 600 of the 100 ms spectra are averaged to give an overall acquisition time of 60 seconds. The LED, optical filter, and peak reflectivity of each channel is reported in Table 2.1.

The currents to the LEDs are regulated to maintain constant temperatures using a custom thermocouple (K type), thermocouple amplifier (Adafruit MAX31856), and thermoelectric cooler (Laird Thermal Solutions 430801-501) PID feedback system controlled by an Arduino Uno. In practice, the LEDs are stabilized to within ±0.03 °C. In the development, it was found that stable control of the temperature of each LED gives a consistent, wavelength-dependent intensity output of the LED and is critical for instrument stability.

Flow limiting orifices are used to control a 10 sccm flow of nitrogen over each mirror to prevent aerosol deposition onto them, thereby ensuring consistent reflectivity. For each cavity a second flow limiting orifice is used to control the flow of sample through the cavity. A total flow

of approximately 350 sccm is used in each cavity as it allows a small residence time (~6 sec) and ensures laminar flow. The total flow pulled for the BBCES is 990 sccm. The pressure and temperature of each cavity are measured with 1 K and 1 hPa resolution using a sensor (Adafruit BME280).

2.2.2 Mirror Reflectivity and Extinction Measurements

The reflectivity of the mirrors and cavity length determine the overall effective pathlength created by the optical cavity. The reflectivity must be determined empirically to transform the changes in integrated intensity to extinction at each wavelength. The mirror reflectivity, R, is measured by measuring the change in intensity when the cavity is flushed with He and N_2:

$$R(\lambda) = 1 - d_0 \frac{\left(\frac{I_{N_2}(\lambda)}{I_{He}(\lambda)}\alpha_{Ray}^{N_2}(\lambda)\right) - (\alpha_{Ray}^{He}(\lambda))}{1-(\frac{I_{N_2}(\lambda)}{I_{He}(\lambda)})} \quad (2.1)$$

In this equation, d_0 is the cavity length, I_x is the integrated intensity when the cavity is purged with Species x, and α_{Ray}^{x} is the scattering coefficient for each species.[15] Monitoring the temperature and pressure allows the number density, N, to be computed from which the scattering coefficient can be calculated using well characterized Rayleigh scattering cross sections, σ.[3, 15]

$$\alpha(\lambda) = N\sigma(\lambda) \quad (2.2)$$

In the reflectivity calibration, the cavity is continually flushed through the mirror purge inlets and one of the sample inlets. A total flow through each cavity is set at 500 sccm, which allows the cavity to be flushed quickly with each sample, and yet remain under laminar flow. Each measurement is saved with a 1-minute acquisition time and it takes approximately 4 minutes to completely purge the cavity of each gas. The cavity remains near atmospheric pressure and temperature during the measurements.

The peak reflectivity for each cavity is 99.984(2), 99.992(3), 99.992(5) at wavelengths 410, 540, and 660 nm. For an empty cavity, effective pathlengths in the range of 0.63 – 3.15 km are achieved. The accuracy of the BBCES-III extinction measurement is dependent on the accuracy of the Rayleigh scattering cross sections of N_2 (1%) and He (1%),[15] the pressure (0.1%) and temperature (0.3%) measurements, and photon counting statistics (0.4%). The uncertainties propagated in quadrature yield an overall measurement uncertainty ranging from 0.9- 2.7%.

For the measurement of Rayleigh Scattering by gases, He was used as the background for each measurement. The extinction was computed using equation 2.3:

$$\alpha(\lambda) = ((\frac{1-R(\lambda)}{d_0})(1 - \frac{I_x(\lambda)}{I_{He(\lambda)}}) + \alpha_{He}(\lambda))(\frac{I_x(\lambda)}{I_{He(\lambda)}}) \quad (2.3),$$

where α represents extinction, d_0 is the length of the cavity, R is the mirror reflectivity, and α_{He} is the Rayleigh scattering by helium.[15]

For aerosol measurements, a small flow of nitrogen is maintained over the mirrors to prevent aerosol deposition and to maintain mirror reflectivity which reduces the distance over which the aerosols interact with the light. This term, r_L, that represents the ratio of the distance of the mirror to mirror separation divided by the distance containing aerosols. This term was determined empirically to be 1.13(5) by measuring the change in extinction by NO_2 measured with and without mirror purges. For laboratory-generated aerosols, the bath gas is N_2 and for ambient aerosol measurements filtered air is the bath gas. Extinction is computed using equation 4.[3]

$$\alpha(\lambda) = r_L(\frac{1-R(\lambda)}{d_0} + \alpha_{bath}(\lambda))(\frac{I_0(\lambda)}{I_{x(\lambda)}} - 1) \quad (2.4)$$

2.2.3 Experimental Set Up

2.2.3.1 Rayleigh Scattering

The experimental set up for measuring Rayleigh scattering by gases is identical to that of the reflectivity measurements using Equation 3. The extinction coefficients of Ar, O_2, and CO_2 at atmospheric pressure and temperature were measured with an acquisition time of 60 seconds. Rayleigh scattering cross sections of Ar and O_2 were computed using n-based calculations. O_2 dimer absorption was modelled using reported cross sections.[15, 23, 24] CO_2 cross sections were taken from the fit provided by He et al.[11] With temperature and pressure measurements, the number density is determined and the theoretical extinction coefficient for each gas is computed.

2.2.3.2 NO_2 Absorption

For further validation purposes, cross sections of NO_2, a strongly absorbing atmospheric pollutant, were measured. A 10.03 ppm standard of a NO_2 /N_2 mixture (Airgas, Inc.) was diluted in N_2 to various concentrations ranging from 156 to 1616 ppt. The I_0 was measured when the cavity was flushed with N_2. To minimize the loss of NO_2, the sample line was purged with a high concentration of NO_2 for 30 minutes before the measurements began.[22]

2.2.3.3 Laboratory Generated Particles

Nigrosin (Sigma Aldrich, CAS# 8005-03-6) aerosols were generated by supplying 3000 sccm of N_2 to a constant output atomizer (TSI 3076). A concentration of 6 g/L provided a lognormal size-distribution with geometric mean near 80 nm and geometric standard deviations near 2.5. The aerosols were dried with two diffusion dryers to give an RH less than 10%. Only 300 sccm was sent through the differential mobility analyzer (DMA), with the excess flow being dumped to waste. The DMA was set to a sheath flow of 3000 sccm, so that the sheath to sample

flow ratio was 10:1. After the DMA, the size-selected aerosol distribution was mixed with 1000 sccm of nitrogen. A volume of 150 cm^3 was found to be appropriate to ensure proper mixing of the size selected aerosols and make-up N_2 before the flow was split between a condensation particle counter (CPC) and the BBCES-III. The size-selected aerosols for nigrosin ranged from 422 nm to 623 nm. In this size regime, a 0.0508 cm impactor with a flow of 300 sccm will to cut all multiply-charged particles, therefore removing the necessity to model their contribution to the extinction cross section. For the Cargille index matching fluid (Cargille Laboratories, L-CABK-1181), the solution was nebulized directly with no dilution. A flow of 300 sccm supplied the nebulizer. The particles produced were diluted by a factor of 100 to yield concentrations of 50-300 particles cm^{-3}.

Measurements of the size-selected aerosols were modelled using Mie theory calculations. A geometric mean of 1.05 was used in the calculations. The input refractive index for Nigrosin was taken from Bluvshtein et al. and was given by the refractive index for the index matching fluid was provided by Cargille.[25] The DMA and CPC were calibrated before the measurements.

2.3. Results

2.3.1 Instrument Sensitivity and Stability

In order to determine the detection limit as a function of acquisition time, the Allan Deviation was calculated for a 6.5 hour time series in which the BBCES-III was purged with N_2. Allan deviation analysis is a common method to determine ideal acquisition rates and to understand how the measurement standard deviation will change as a function of integration time.[14] Under the inert conditions, deviations in the integrated intensity are due to instrumental noise and drift. The major source of drift is attributed to the varying output of the LED. A secondary source of noise is the photon counting by the spectrophotometer. White (random)

noise will cancel by averaging; therefore, measurement standard deviation for a system with only white noise will decrease by $1/\sqrt{n}$, where n equals the number of samples.[14] In addition to white noise, the instrument is subject to drift. Once the impact of the drift becomes substantial, increasing the integration time does not improve measurement standard deviation.

In the Allan deviation analysis, each 100 ms spectra was averaged 10 times to give 24408 spectra with 1 second acquisition time. The spectra are converted to extinction and overlapping Allan Deviation was calculated on the extinction time series. The Allan Deviation analysis identified that an optimum sampling time for the BBCES-III occurs near 100 seconds and yields ultimate detection limits of 0.04, 0.03, and 0.06 Mm^{-1} at 406, 532, and 662 nm. However, measurements with such short integration times are not practical as they reduce the sampling rate by requiring frequent background measurements. To determine the detection limit for this routine, an additional analysis was performed on the same data set. In this analysis, a 2-minute background is recorded and the remaining 28 minutes of data are transformed into extinction values. The standard deviation of the extinction values across the timeseries is computed. With a 1 second acquisition time for the sample measurements, the 3σ detection limit is 0.76, 0.92, and 1.3 Mm^{-1} at 406, 532, and 662 nm. Increasing the averaging time to 1 minute significantly improves the detection limits to 0.34, 0.30, and 0.48 Mm^{-1}. (Figure 2.2)

2.3.2 Validation

The instrument accuracy was verified using a variety of gases and laboratory-generated aerosols. Validation experiments include extinction measurements of Rayleigh scattering by argon, oxygen, and carbon dioxide, as well as NO_2 absorption cross section, and the extinction cross section of laboratory-generated aerosols; including measurement of purely scattering

particles, consisting of Cargille Index matching fluid, and absorbing particles consisting of Nigrosin.

2.3.2.1 Rayleigh Scattering

Rayleigh scattering by argon, carbon dioxide, and oxygen were measured by the BBCES-III, as shown in Figure 2.3. The extinction measurements are compared to theoretical rayleigh scattering cross sections from Thalman et al. for Ar and O_2 and the fit provided by He et al. for CO_2.[11, 15] The residuals are generally <1 Mm^{-1} exhibiting great agreement between the BBCES-III measurements and theory. There are numerous Rayleigh scattering cross sections, we have chosen to compare to the theoretical refractive index n-based cross sections of argon and oxygen due to agreement.[15] N-based for CO_2 exhibited larger residuals than the power law fit provided by He et al. consequently the data is shown in reference to He et al.[11] The O_2 measurements show larger deviation from theory where O_2-O_2 absorption bands occur.[23, 24] These deviations likely result from errors in the calculated O_2-O_2 number densities since they are quadratically dependent on the O_2 number densities. The good agreement between the measurements and the literature values demonstrate the capability of the BBCES-III for measuring extinction across the spectrum.

2.3.2.2 Absorbing Gas

The absorption cross section of NO_2 was measured using the BBCES-III in five sets of measurements. The cross section (σ) of each dataset was determined by performing a linear regression of extinction vs number density of NO_2 for each wavelength. The linear response and dynamic range of the instrument was highlighted in the measurements. The absorption cross section of NO_2 spans three orders of magnitude in the BBCES-III measurement range. A variety

of concentrations could be captured in single dataset, yielding extinction values from 2 up to 1938 Mm^{-1}. All fits had R^2 values greater than 0.994 for the linear regression of extinction vs number density of NO_2. The averaged measured absorption cross sections are shown in Figure 2.4, along with the absorption cross section reported by Burrows et al.[22] The error bars represent the standard deviation among the five data sets. Among the literature datasets of NO_2, discrepancies are apparent in the red spectral region (BBCES-III cavity 635-685 nm). Greatest agreement with residuals is seen with the cross section reported by Burrows et al.[22]

2.3.2.3 Laboratory-Generated Aerosols

The previous validation steps have focused on gas phase measurements of well-defined species. This instrument however, is intended to measure ambient aerosol extinction. To justify the BBCES-III ability to quantitatively measure aerosol extinction, laboratory generated aerosols were measured. A laboratory generated aerosol with a well characterized refractive index is Cargille Index Matching fluid, which was nebulized into aerosol particles in order to specifically validate the scattering accuracy of the BBCES-III. Particles ranging from 681 - 779 nm were sampled in 20 nm increments. The measured extinction cross section of Cargille Index Matching fluid along with the theoretical cross sections modelled from Mie theory are shown in Figure 2.5 and have good agreement. The errors associated with these measurements are all within the uncertainties that were propagated. These measurements when compared to the Mie theory cross section calculations gave residuals ranging from -9 to 5% with a root-mean-square error of 2.12.

The extinction of the commonly studied laboratory generated aerosol of nigrosin was measured by the BBCES-III. The measured extinction cross section as well as theoretical extinction cross section from Mie theory are shown in Figure 2.6. The measured extinction cross section shows excellent agreement with modelled values for nigrosin. All measurement error is

within the propagated uncertainty. Residuals between measured and modelled cross sections ranged from -10 to 4% and have a root-mean-square error of 2.34. Error bars are omitted from the plot for clarity. Propagation of the measurement uncertainty on the 1-minute average extinction spectra and concentration measurement gave an uncertainty ranging from 6.7 to 11.2%. These larger residuals can be due to errors associated with the DMA and CPC that were not fully corrected by the calibration before the particle measurements. The propagated uncertainties do not take include contributions from uncertainties in the refractive indices. Along with the fact that these residuals all fall within expected uncertainties it is still acceptable to say that the BBCES-III provides precise aerosol extinction measurements. Therefore, the validation of the BBCES-III is further confirmed by these laboratory-generated aerosol measurements.

2.3.3 Application: Ambient Aerosol Measurements

The BBCES-III was developed to monitor ambient aerosol extinction. From November 24, 2018 at 21:00:00 through November 25 at 12:00:00, the BBCES-III sampled ambient aerosols drawn from outside of the Chemistry building at the University of Georgia. This extinction time series is shown in Figure 2.7. An automated routine controlled a pinch valve (NResearch 648P093-62) to switch between lines with and without a HEPA filter on a 6:24 minute cycle. An I0 was defined as a 2-minute average of the filtered air measurements. Each sample spectrum was recorded with an acquisition time of 1 minute. A diffusion dryer was used during the experiment and the RH was kept below 30%. The mirror reflectivity was measured before and after the experiment and determined to be constant.

In addition to the BBCES-III, the MultiPAS-IV, a 4 wavelength (406, 532, 662, 780 nm) photoacoustic spectrometer, and 2 cavity ringdown spectrometers (445 and 662 nm) were operated. The cavity ringdown spectrometers provided an alternate extinction measurement to

further examine the BBCES-III accuracy. Agreement with the 662 nm CRD and 662 nm BBCES-III measurement was within 3% with an R^2 of 0.98 and agreement with the 445 nm CRD and an extrapolated 445 nm BBCES-III measurement was within 4% with an R^2 value of 0.91, this correlation is exhibited in Figure 2.9. Clearly excellent agreement between the direct measurement at 662 nm and the fitted extinction value at 445 nm is seen with the alternative extinction measurement by the CRDs.

Over this time series, the BBCES-III extinction measurements were fit to a power law yielding the EAE. With over 120 nm of the UV-Vis spectrum covered from 385-690 nm, there is great certainty on the Extinction Ångström Exponents measured. As shown in Figure 2.10, variability in the EAE was seen with values ranging from 1.6 to 2.8 over this measurement period.

With the absorption data from the MultiPAS-IV, the Single Scattering Albedo (SSA) of each measurement was computed at 406, 532, and 662 nm. As shown in Figure 2.11, SSA values exhibited variability in both magnitude and spectral shape. For example, some measurements had SSA values up to 0.95 with virtually no wavelength dependence, whereas other spectra were observed with an inverse relationship with wavelength; ie. the 406 nm measurement at 0.88 and the 662 nm measurement at 0.83. Variability in SSA can be explained by different particle types, this phenomenon has been explored by Li et al. where the wavelength dependence of SSA was shown to vary depending on the composition of the aerosol.[7] With the combination of a 4 wavelength PAS and the BBCES-III, we have distinguished capabilities to measure the wavelength dependence of the SSA of aerosols.

2.4. Conclusions

The BBCES-III improves upon existing broadband cavity-enhanced spectrometers by providing large spectral coverage. To the author's knowledge, this instrument provides spectral coverage that is only comparable to the design by He et al.[11] The BBCES-III multi-cavity design is an alternative approach to achieving broad spectral coverage. This design is modular and by simply changing the LED and optical components, different wavelength ranges can be targeted. The wavelength ranges chosen for the BBCES-III allow for measurements to explore the wavelength dependence of many aerosol optical properties.

This instrument was developed to be utilized and modified to aid in aerosol characterization of ambient and laboratory generated aerosols. The small footprint of the BBCES-III provides ease of transportation and would be ideal for portability. Future application of the BBCES-III would be to further characterize refractive indices of laboratory generated particles because of our unique ability to cover a large part of the UV- Visible spectrum. Furthermore, the BBCES-III partnered with the MultiPAS-IV allows for the differentiation of SSA wavelength dependence which can indicate different types of particles. This phenomenon can allow for ambient aerosol classification, which can be helpful in predicting radiative forcing of different sources.

Chapter 2 Figures

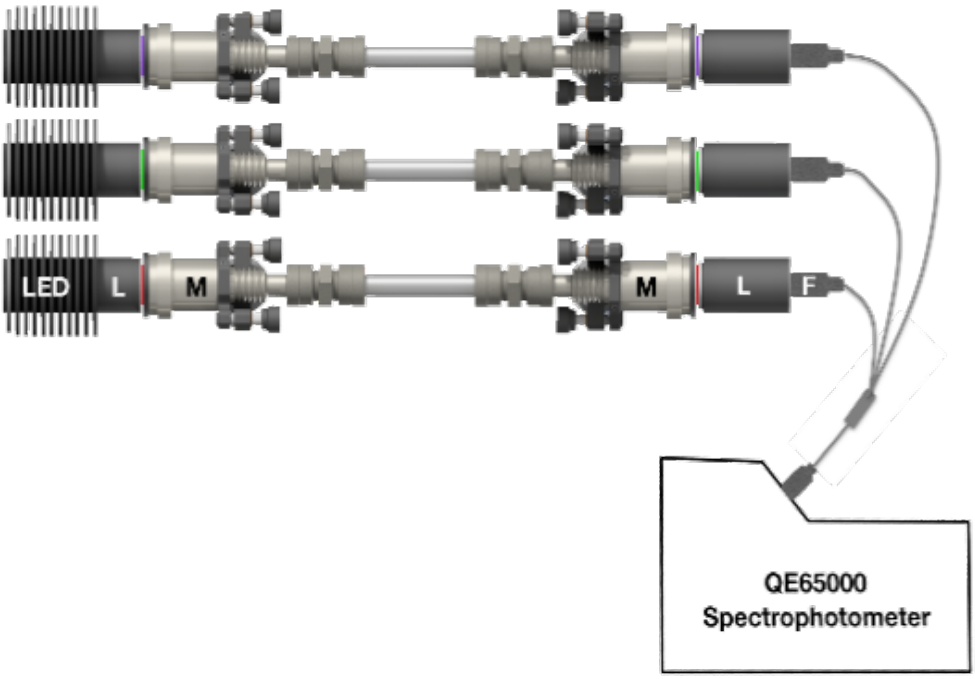

Figure 2.1. The BBCES-III

A schematic of the BBCES-III. L = lens, M = mirror. F = fiber optic. S = spectrophotometer

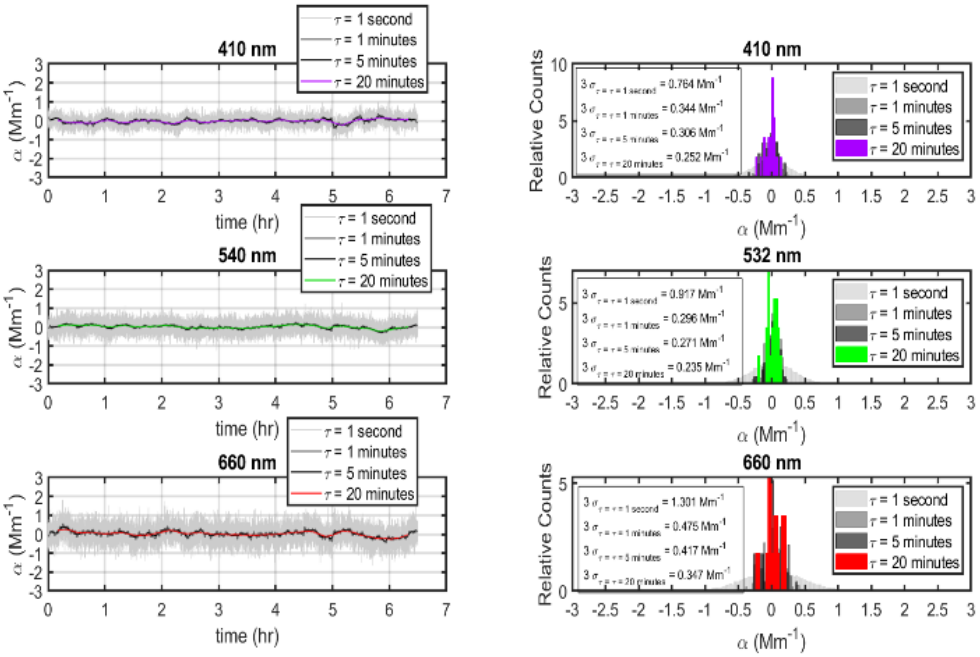

Figure 2.2a. Allan Deviation Timeseries

Figures a-c show the extinction time series in the Allan deviation experiment for 6.5 hours. Figures d-f are histograms corresponding to the varying extinction value over the time series.

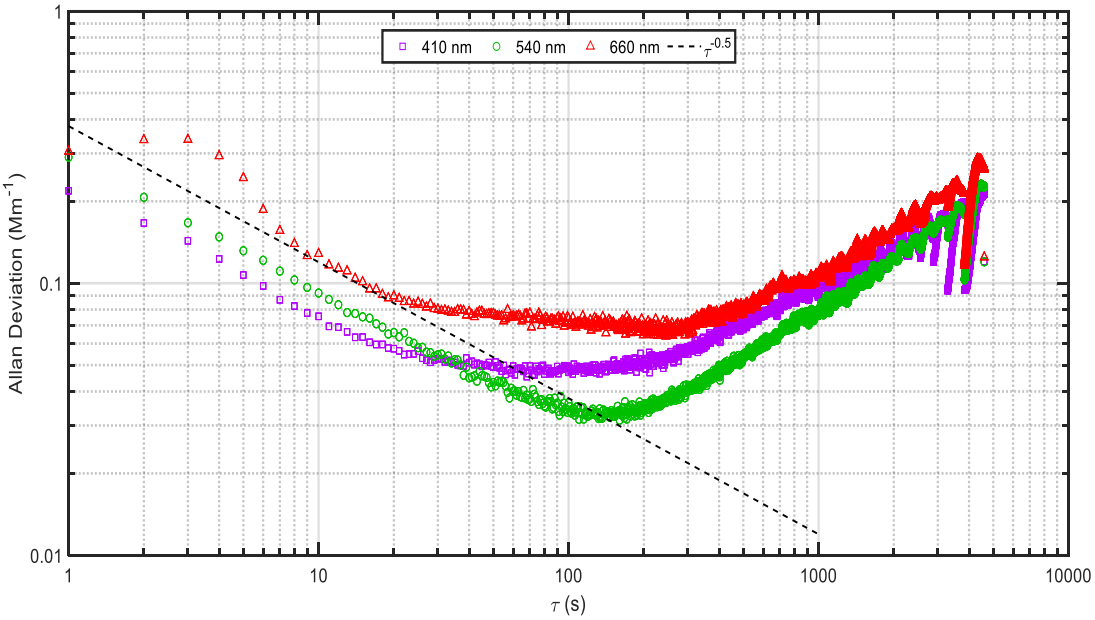

Figure 2.2b. Allan Deviation Results

Shows the Allan deviation results of a 6.5 hour time period for wavelengths 410, 540, and 660 nm.

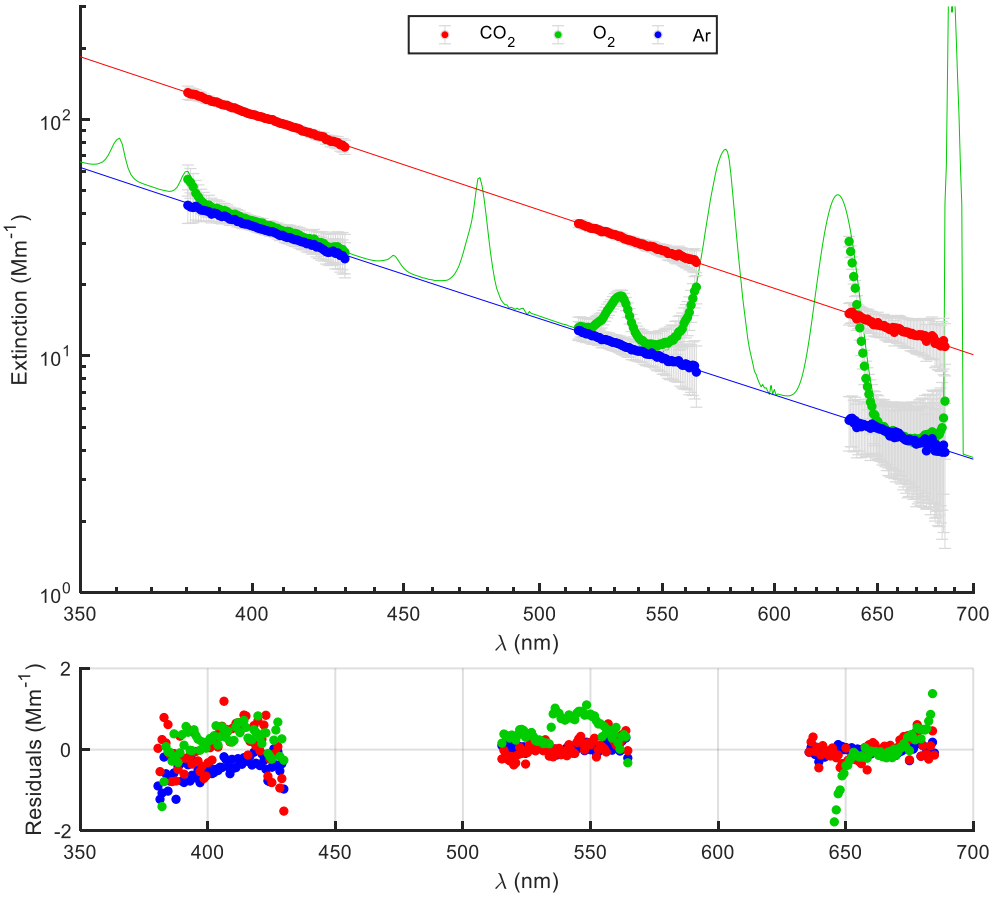

Figure 2.3. Rayleigh Scattering Extinction Spectra

Figure 2.3a. Rayleigh scattering gases extinction spectra measured by the BBCES-III, along with theoretical extinction spectra computed using n-based calculations. A log-log scale was used to highlight the low values of extinction at longer wavelengths

Figure 2.3b. Residuals in Mm^{-1} of the BBCES-III measurements compared to theoretical extinction.

Red= CO_2 Green= O_2 Blue= Ar

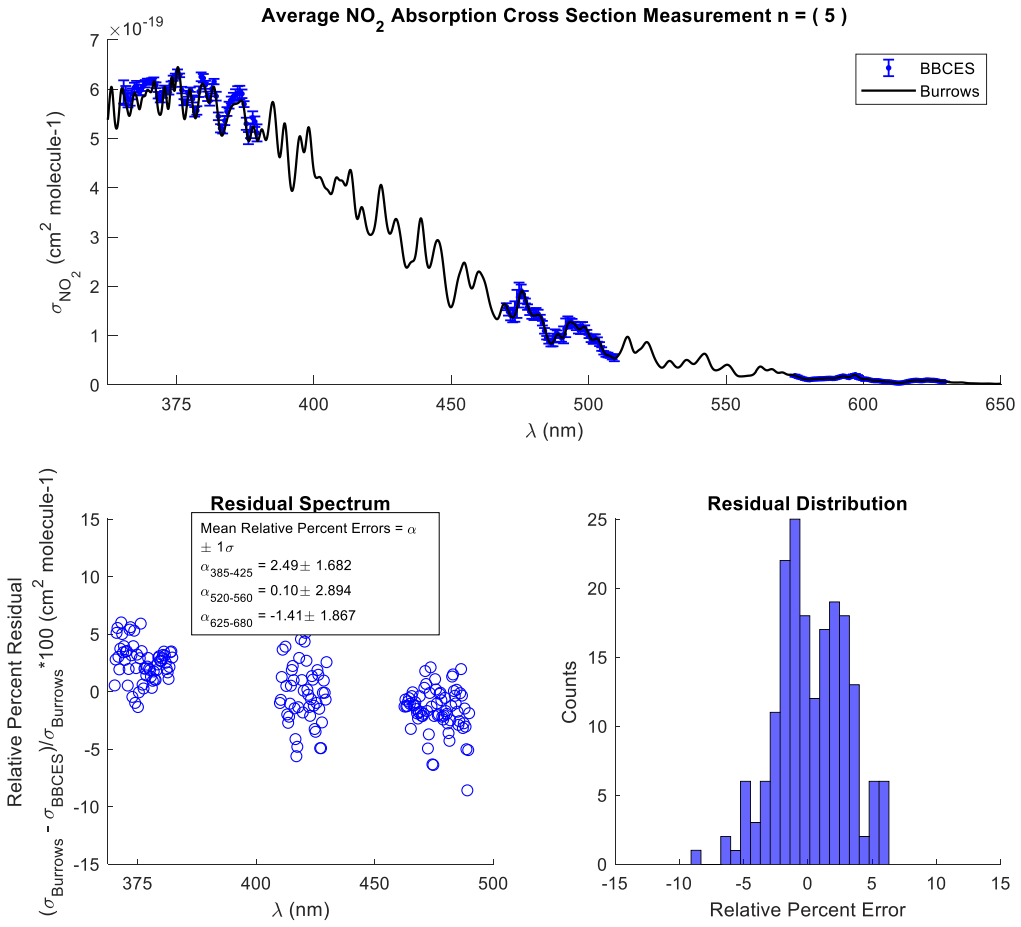

Figure 2.4. NO_2 Measurements by the BBCES-III

Figure 2.4a shows the average of 5 NO_2 absorption cross section measurements from the BBCES-III overlaid with Burrows measurements.

Figure 2.4b shows the relative percent residual for these measurements, with the mean relative percent errors all being within 9 percent.

Figure 2.4c exhibits the residual distribution as a histogram using all the BBCES-III reported wavelengths. The residuals are largely centered around 0 and have a relative percent error within 10% for all wavelengths.

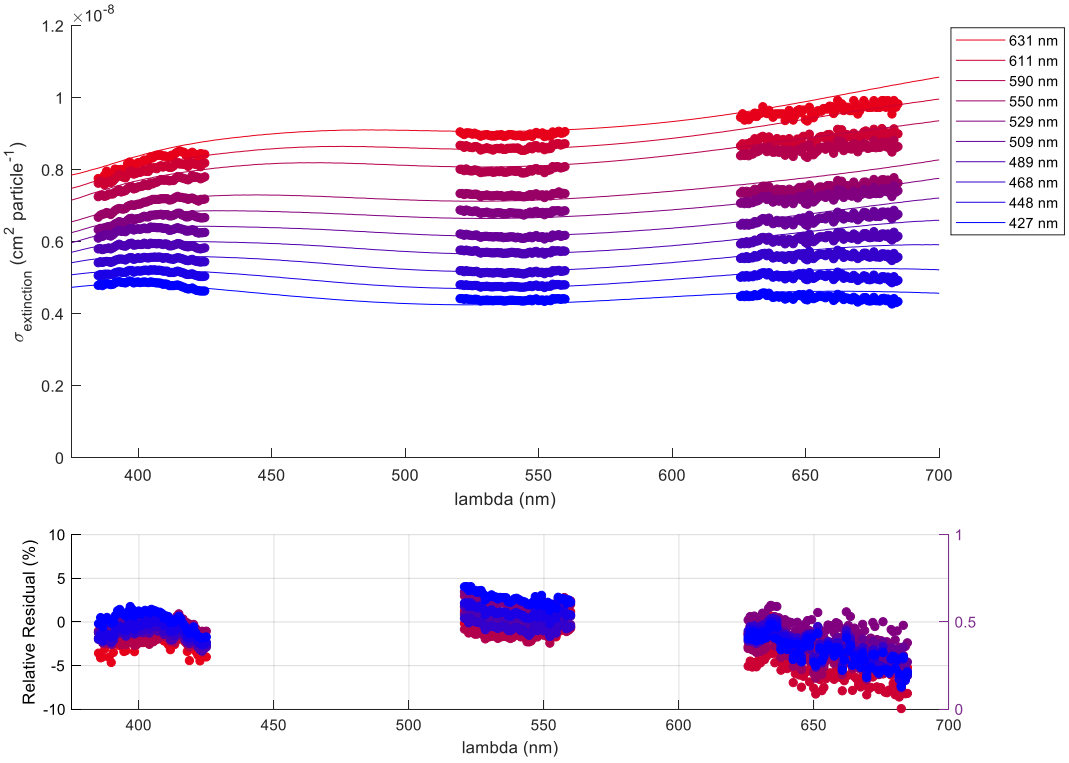

Figure 2.5. Nigrosin Extinction Cross Section Measurements

The extinction cross section of Nigrosin is reported at particle sizes ranging from approximately 430 to 630 nm in 20 nm increments. These cross sections are compared to theoretical cross sections that are calculated using Mie theory.

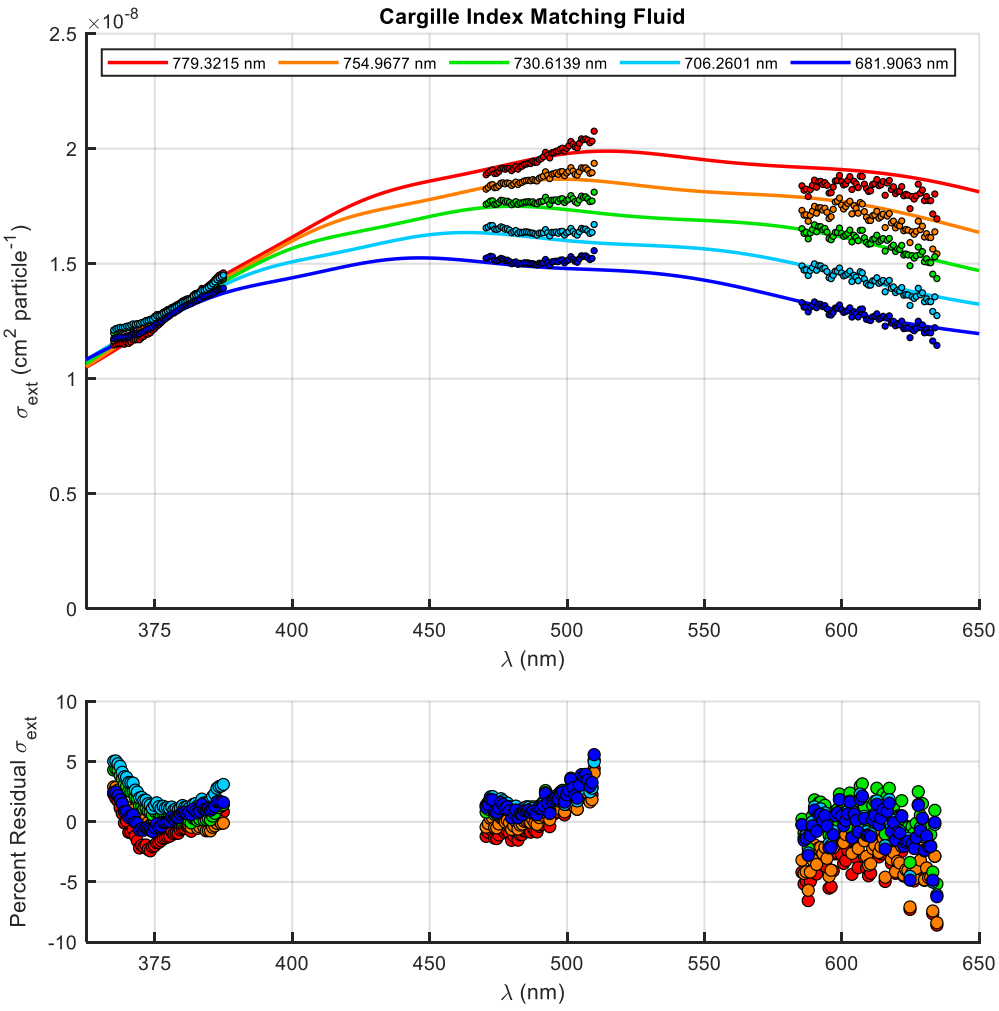

Figure 2.6. Cargille Extinction Cross Section Measurements

The BBCES- III measured extinction cross sections of Cargille Index matching fluid from a range of particle sizes, along with the Mie theory calculated extinction cross sections.

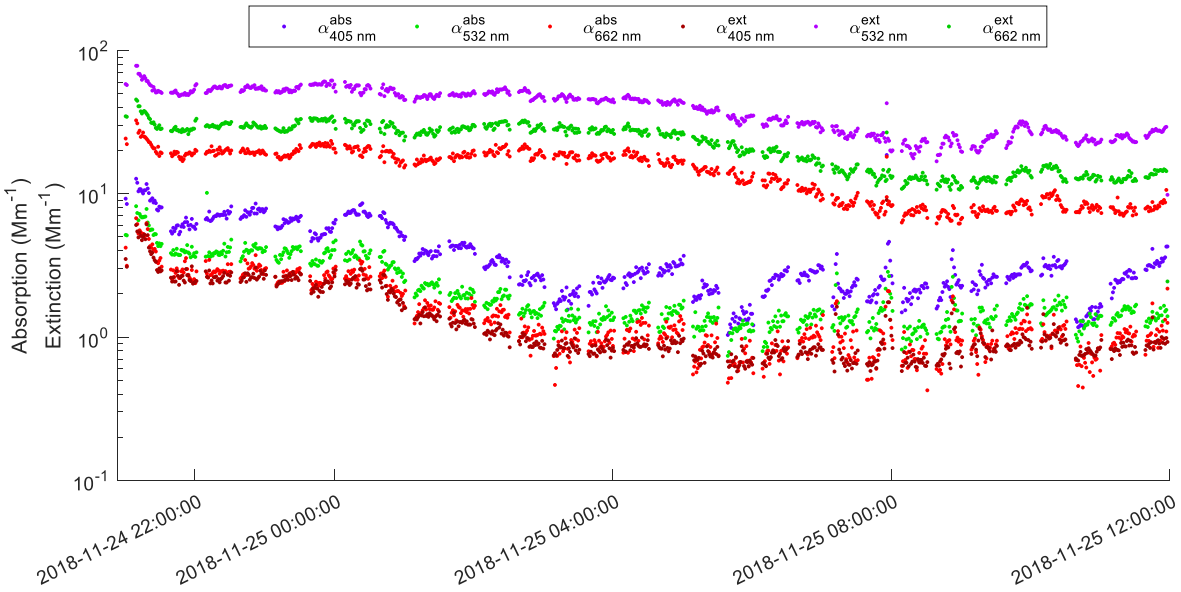

Figure 2.7. Ambient Timeseries

The ambient timeseries with measured extinction over time from the BBCES-III at wavelengths 405, 532, and 662 nm. Additionally, the absorption measurements from the MultiPAS-IV with wavelengths at 406, 532, 662, and 780 nm are displayed.

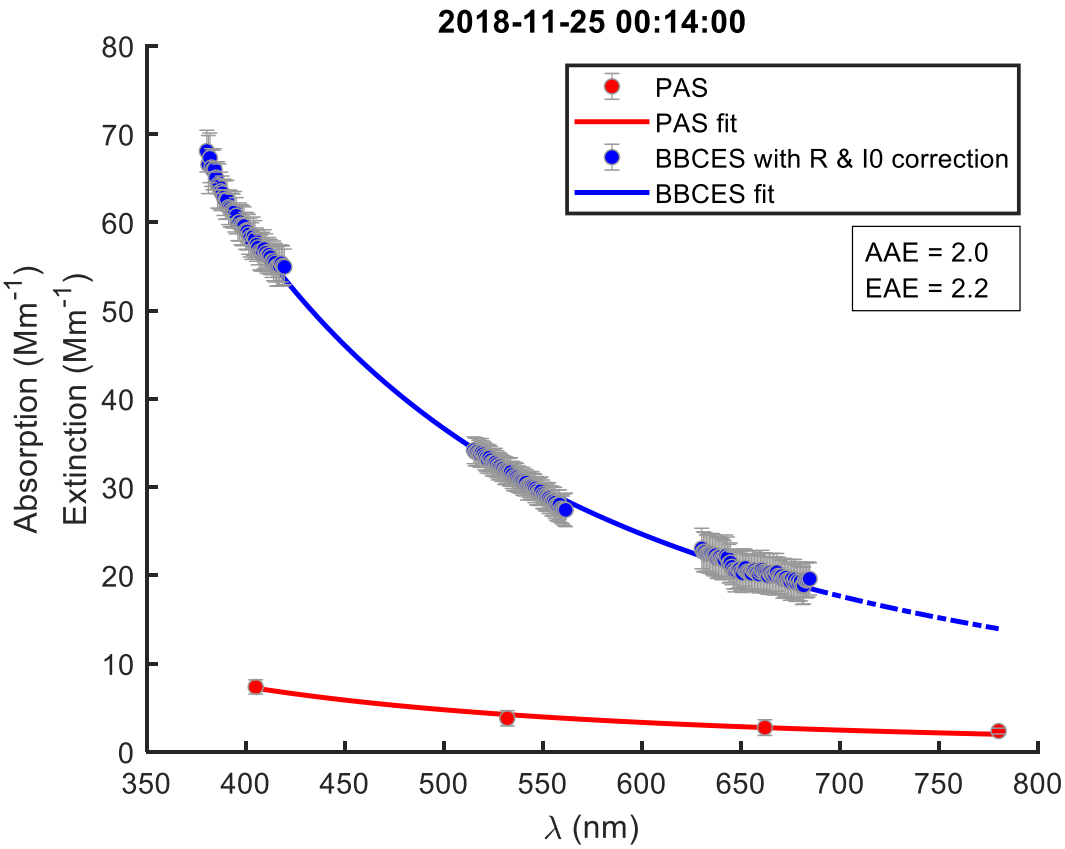

Figure 2.8. An Ambient Extinction and Absorption Spectrum

A typical absorption and extinction spectrum from the ambient data set.

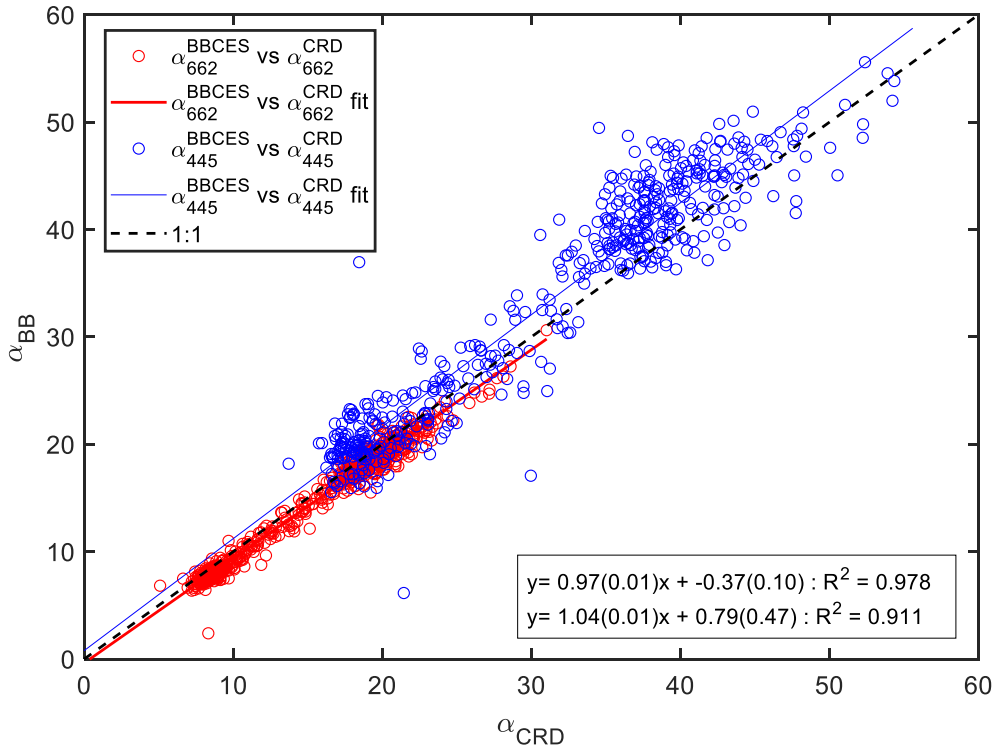

Figure 2.9. Extinction Correlation between CRD and BBCES-III

Measured extinction from BBCES-III at 662 nm correlated with 662 nm CRD spectrometer (red). Also displayed is a 445 nm extinction value interpolated from BBCES-III EAE fit correlated with measured extinction from 445 nm CRD spectrometer (blue).

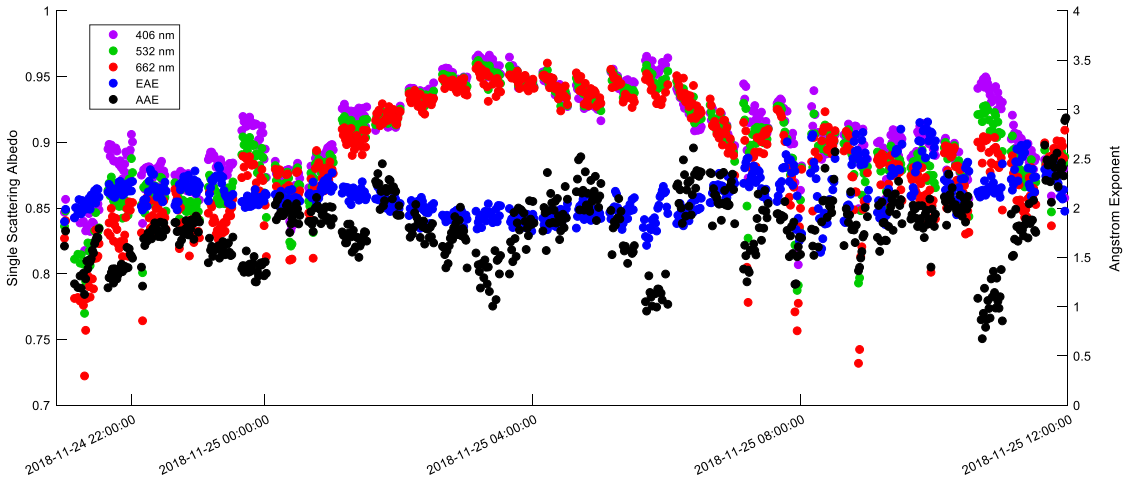

Figure 2.10. Timeseries of Ambient SSA, EAE, and AAE

The SSA 406, 532, 662 nm as a function of time. Additionally, on the right Y axis the EAE and AAE are displayed and represented by the blue and black points respectively.

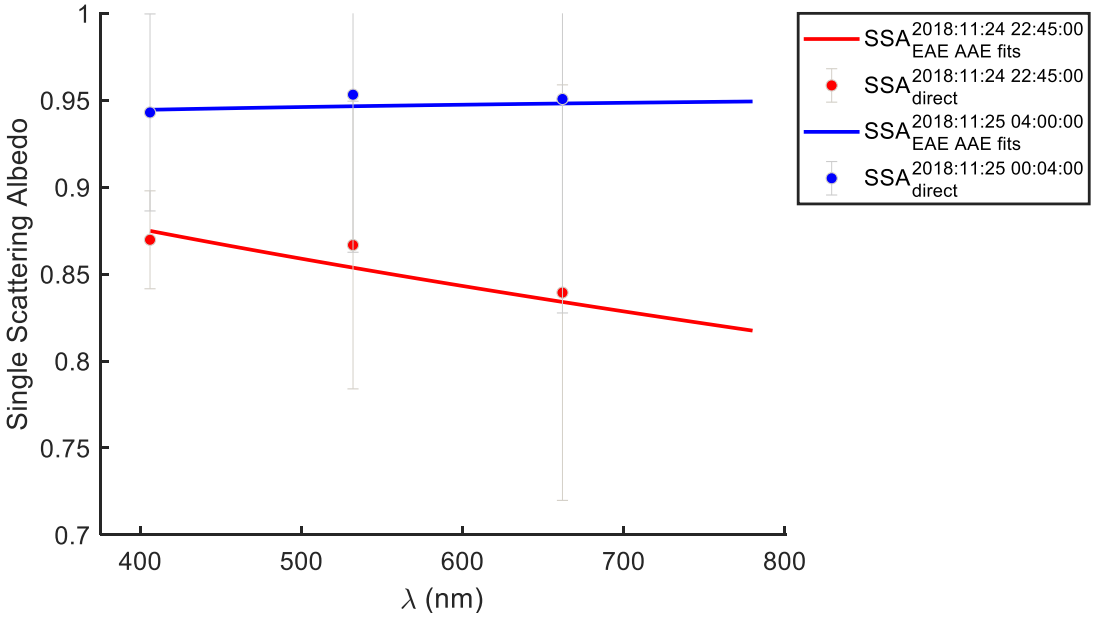

Figure 2.11. Wavelength dependent SSA of Ambient Aerosols

Direct measurements of the Single Scattering Albedo of ambient data at 406, 532, and 662 nm shown in points. Additionally, the SSA spectrum was computed from 406- 780 nm using the EAE and the AAE fit.

Table 2.1. Relevant Optical Equipment for the BBCES-III

Channel	LED	Optical filter	Measured Peak Reflectivity and center wavelength
UV 385-425 nm	LZ1-10UB00-01U7, (LED ENGIN)	450SP RAPIDEDGE (OMEGA Optical)	99.984(2) at 410 nm
Green 520- 560 nm	LZ1-00G100, (LED ENGIN)	FF01-540/50, (Semrock)	99.992(3) at 540 nm
Red 630- 685 nm	XPLAWT-00-0000-000HU60E8-BS01, (Opulent)	660BP8-RAPIDBAND, (OMEGA Optical)	99.992(5) at 660 nm

References

1. IPCC, 2013: *Climate Change 2013: The Physical Science Basis. Contribution of Working Group I to the Fifth Assessment Report of the Intergovernmental Panel on Climate Change* [Stocker, T. F., D. Qin, G. K. Plattner, M. Tignor, S.K. Allen, J. Boschung, A. Nauels, Y. Xia, V. Bex and P. M. Midgley (eds.)]. Cambridge University Press, Cambridge, United Kingdom and New York, NY, USA, 1535 pp, doi:10.1017/CBO9781107415324.
2. McComiskey, A.; Schwartz, S. E.; Schmid, B.; Guan, H.; Lewis, E. R.; Ricchiazzi, P.; Ogren, J. A. Direct Aerosol Forcing: Calculation from Observables and Sensitivities to Inputs. *J. Geophys. Res.* **2008**, *113* (D9), D09202. https://doi.org/10.1029/2007JD009170.
3. Washenfelder, R. A.; Flores, J. M.; Brock, C. A.; Brown, S. S.; Rudich, Y. Broadband Measurements of Aerosol Extinction in the Ultraviolet Spectral Region. *Atmos. Meas. Tech* **2013**, *6*, 861–877. https://doi.org/10.5194/amt-6-861-2013.
4. Nilsson, B. Meteorological Influence on Aerosol Extinction in the 02–40-Mm Wavelength Range. *Appl. Opt.* **1979**, *18* (20), 3457. https://doi.org/10.1364/AO.18.003457.
5. Suzuki, K.; Takemura, T. Perturbations to Global Energy Budget Due to Absorbing and Scattering Aerosols. *J. Geophys. Res. Atmos.* **2019**, *124* (4), 2194–2209. https://doi.org/10.1029/2018JD029808.
6. Bond, T. C.; Bergstrom, R. W. Light Absorption by Carbonaceous Particles: An Investigative Review. *Aerosol Science and Technology*. January 1, 2006, pp 27–67. https://doi.org/10.1080/02786820500421521.

7. Li, J.; Carlson, B. E.; Lacis, A. A. Using Single-Scattering Albedo Spectral Curvature to Characterize East Asian Aerosol Mixtures. *J. Geophys. Res.* **2015**, *120* (5), 2037–2052. https://doi.org/10.1002/2014JD022433.
8. Schuster, G. L.; Dubovik, O.; Holben, B. N. Angstrom Exponent and Bimodal Aerosol Size Distributions. *J. Geophys. Res.* **2006**, *111* (D7), D07207. https://doi.org/10.1029/2005JD006328.
9. Andreae, M. O.; Gelencsér, A. *Atmospheric Chemistry and Physics Black Carbon or Brown Carbon? The Nature of Light-Absorbing Carbonaceous Aerosols*; 2006; Vol. 6.
10. Anderson, T. L.; Ogren, J. A. Determining Aerosol Radiative Properties Using the TSI 3563 Integrating Nephelometer. *Aerosol Sci. Technol.* **1998**, *29* (1), 2957–2969. https://doi.org/10.1080/02786829808965551.
11. He, Q.; Bluvshtein, N.; Segev, L.; Meidan, D.; Flores, J. M.; Brown, S. S.; Brune, W.; Rudich, Y. Evolution of the Complex Refractive Index of Secondary Organic Aerosols during Atmospheric Aging. **2018**. https://doi.org/10.1021/acs.est.7b05742.
12. Jordan, C. E.; Anderson, B. E.; Beyersdorf, A. J.; Corr, C. A.; Dibb, J. E.; Greenslade, M. E.; Martin, R. F.; Moore, R. H.; Scheuer, E.; Shook, M. A.; et al. Spectral Aerosol Extinction (SpEx): A New Instrument for in Situ Ambient Aerosol Extinction Measurements across the UV/Visible Wavelength Range. *Atmos. Meas. Tech.* **2015**, *8* (11), 4755–4771. https://doi.org/10.5194/amt-8-4755-2015.
13. Galpin, T.; Chartier, R. T.; Levergood, N.; Greenslade, M. E. Refractive Index Retrievals for Polystyrene Latex Spheres in the Spectral Range 220–420 Nm. *Aerosol Sci. Technol.* **2017**, *51* (10), 1158–1167. https://doi.org/10.1080/02786826.2017.1339014.

14. Langridge, J. M.; Ball, S. M.; Shillings, A. J. L.; Jones, R. L. A Broadband Absorption Spectrometer Using Light Emitting Diodes for Ultrasensitive, in Situ Trace Gas Detection. *Rev. Sci. Instrum* **2008**, *79*, 123110. https://doi.org/10.1063/1.3046282.

15. Thalman, R.; Zarzana, K. J.; Tolbert, M. A.; Volkamer, R. Rayleigh Scattering Cross-Section Measurements of Nitrogen, Argon, Oxygen and Air. *J. Quant. Spectrosc. Radiat. Transf.* **2014**, *147*, 171–177. https://doi.org/10.1016/J.JQSRT.2014.05.030.

16. Zhao, W.; Dong, M.; Chen, W.; Gu, X.; Hu, C.; Gao, X.; Huang, W.; Zhang, W. Wavelength-Resolved Optical Extinction Measurements of Aerosols Using Borad-Band Cavity-Enhanced Absorption Spectroscopy over the Spectral Range of 445-480 Nm. *Anal. Chem* **2013**, *85*, 43. https://doi.org/10.1021/ac303174n.

17. Ball, S. M.; Langridge, J. M.; Jones, R. L. Broadband Cavity Enhanced Absorption Spectroscopy Using Light Emitting Diodes. https://doi.org/10.1016/j.cplett.2004.08.144.

18. Zheng, K.; Zheng, C.; Zhang, Y.; Wang, Y.; Tittel, F.; Wang, Y.; Tittel, F. K. Review of Incoherent Broadband Cavity-Enhanced Absorption Spectroscopy (IBBCEAS) for Gas Sensing. *Sensors* **2018**, *18* (11), 3646. https://doi.org/10.3390/s18113646.

19. Engeln, R.; Von Helden, G.; Berden, G.; Meijer, G. Phase Shift Cavity Ring down Absorption Spectroscopy. *Chem. Phys. Lett.* **1996**, *262* (1–2), 105–109. https://doi.org/10.1016/0009-2614(96)01048-2.

20. Fischer, D. Al; Smith, G. D. A Portable, Four-Wavelength, Single-Cell Photoacoustic Spectrometer for Ambient Aerosol Absorption. *Aerosol Sci. Technol.* **2018**, *52* (4), 393–406. https://doi.org/10.1080/02786826.2017.1413231.

21. Kebabian, P. L.; Robinson, W. A.; Freedman, A. Optical Extinction Monitor Using CW Cavity Enhanced Detection. *Rev. Sci. Instrum* **2007**, *78*, 63102. https://doi.org/10.1063/1.2744223.

22. J.P. Burrows, A. Dehn, B. Deters, S. Himmelmann, A. Richter, S. Voigt, and J. Orphal, "Atmospheric remote-sensing reference data from GOME: Part 1. Temperature-dependent absorption cross-sections of NO_2 in the 231-794 nm range", J. Quant. Spectrosc. Radiat. Transfer 60, 1025-1031 (1998); DOI: 10.1016/S0022-4073(97)00197-0

23. Thalman, R.; Volkamer, R. Temperature Dependent Absorption Cross-Sections of O2-O 2 Collision Pairs between 340 and 630 Nm and at Atmospherically Relevant Pressure. *Phys. Chem. Chem. Phys.* **2013**, *15* (37), 15371–15381. https://doi.org/10.1039/c3cp50968k.

24. Greenblatt, G. D.; Orlando, J. J.; Burkholder, J. B.; Ravishankara, A. R. Absorption Measurements of Oxygen between 330 and 1140 Nm. *J. Geophys. Res.* **1990**, *95* (D11). https://doi.org/10.1029/jd095id11p18577.

25. Bluvshtein, N.; Michel Flores, J.; He, Q.; Segre, E.; Segev, L.; Hong, N.; Donohue, A.; Hilfiker, J. N.; Rudich, Y. Calibration of a Multi-Pass Photoacoustic Spectrometer Cell Using Light-Absorbing Aerosols. *Atmos. Meas. Tech.* **2017**, *10* (3), 1203–1213. https://doi.org/10.5194/amt-10-1203-2017.

CHAPTER 3

OPTIMAL LED PARAMETERIZING AND TROUBLESHOOTING

Broadband Optimization

During the development of the BBCES-III there were many different alterations that were done in order to maximize the efficiency and stability of the instrument. The light sources of the LEDs are a crucial aspect of this instrument and therefore the stability of their intensity directly correlates to the ability of the BBCES-III to measure extinction accurately. Here the optimization of the temperature control of the LEDs is discussed and shown to have improved over this trouble shooting process. Next the actual LEDs that were chosen to be the light sources for the BBCES-III were examined and evaluated to see which LED would best serve the purpose needed by this instrument. These alterations have shown to improve the signal and stability of the BBCES-III.

3.1 Introduction

The light sources of the BBCES-III are three LEDs, one for each cavity. They each are specifically selected to be partnered with the dielectric coating that is on each mirror of each of the cavities.[1] For example, the peak reflectivity of the UV cavity is 410 nm and the LED for that cavity is reported to be 405-410 nm. Stability of the LED output is a major factor in the efficiency of the BBCES-III. Factors that can affect LED stability are the temperature of the LED baseplate and the stability of the power source driving the LED. The temperature of the LED must be managed as ambient temperature fluctuations will affect the temperature of the LED baseplate, thus altering the stability.[2]

The peak of the spectral shape of the LED output shifts with temperature fluctuations causing the intensity of this LED to shift. LED manufacturers include these shifts in intensity and temperature to show how stable or unstable the LED is as a result of temperature. Shown in Figure 3.1 is the intensity shift as a result of temperature for the green LED of the BBCES-III. This almost 2 nm shift as a result of a change of 20 °C shows how it is necessary to control this temperature in order to maintain a constant output.[3]

For the BBCES-III temperature control is maintained by a K-type thermocouple temperature sensor that is placed onto the LED and an Arduino. The Arduino sends commands to a thermoelectric cooler placed behind the LED base plate that cools based on the feedback from the thermocouple. Through this feedback loop, temperature stability is maintained. The temperature at which each LED is maintained is selected based on the natural temperature of the LED; the aim is to have the thermoelectric coolers constantly cooling but not at the full power setting of the thermoelectric cooler. Using these parameters, the original BBCES-III set up had selected 35 °C for the green and UV cavities, and 45 °C for the red cavity. As a result of this feedback setup the BBCES-III is highly dependent on the temperature and reaction time of the thermoelectric cooler.

The original LED temperature control setup of the BBCES-III had some issues that affected the performance of the BBCES-III. These were made apparent by standard deviations of raw intensity taken over the course of varying time points all of which were at least over an hour. The standard deviation of the intensity is taken from the mean of the intensity over that time period. This allows for the changes in intensity to be shown as a function of wavelength where drift truly affects the results, which is the similar to the purpose of the Allan deviation experiments.[4] Figure 3.2 below exhibits a typical result of this experiment. As shown in this

figure, the UV LED had some stability issues, which was attributed to the age of the LED and the gradual degradation of the performance of the LED.[5]

Also shown in Figure 3.2 is a large amount of scatter in the red cavity. This was originally attributed to there being low LED signal in the red cavity. The LED that was being used in the red cavity was XPLAWT-00-0000-000HU60E8-SB01(Opulent) which is a white LED that was filtered using an Opulent filter to give wavelengths 635- 685 nm, so the intensity was considerably lower in that cavity than in the two others. This was originally what was assumed to be the issue with the large deviation in that cavity. As a result, it was hoped that replacing the white LED with a red LED would increase the light intensity.

A separate issue with temperature control was with the green cavity thermocouple. Relatively often the green thermocouple would lose connection and give NaN results as the raw data from the thermocouple. This would cause the thermocooler to be beyond its highest power output and the temperature of the LED would thus be decreased and the intensity of the LED would be affected. The temporary solution was to adjust the connection to the Arduino until the connectivity issues had been resolved and the thermocouple was again reading the appropriate temperature. This was not an ideal scenario during data collection as the temperature control is crucial for an accurate measurement. This resulted in many experiments that had to be repeated, so this had to be addressed in the instrument troubleshooting process.

Potential solutions for optimizing the intensity output of the LEDs were discussed and it was decided that purchasing new LEDs would be a good first step in improving the light sources. One of these changes was to try a red LED in the red cavity instead of a white LED in hopes that the LED would have a higher intensity in the red spectral region, thus creating a more precise reading in the red cavity. Another solution to aiding with stable LED output was to address the temperature fluctuations by updating the Arduino board to react to smaller temperature

fluctuations.[6] The hope was that with better precision on the temperature regulating loop, the intensity would be more stable and that the standard deviation of all the cavities would improve. An extension of this was to modify PID loop settings of each LED to be optimized for this temperature regulating loop. This was hoped to minimize oscillation time that was required after an external temperature change.

A PID loop is a form of a control loop, used to adjust something based on previous products. The PID loop uses a setpoint and a feedback to determine how far away from that set point the desired results are. The acronym PID stands for proportional, integral, and derivative, using these different variables the goal of this control loop is to eliminate the error between the setpoint and the feedback.[7,8]

3.2 Thermal troubleshooting

The original thermocouple amplifier board was an Arduino thermocouple amplifier MAX31855.[9] This amplifier board in practice gave thermal readings to the nearest 0.25 °C. This proved to not necessarily be the best way to thermally regulate the LEDs. The PID loop that controls the thermal coolers would only activate when the temperature change was larger than 0.25 °C. This allowed for small fluctuations in temperature that were less than 0.25 °C and thus small fluctuations in intensity from the LEDs. A new thermocouple amplifier board was purchased, an Adafruit MAX31856 Universal Thermocouple Amplifier.[10] This new amplifier board in practice controlled the temperature within 0.03 °C, which allowed for the PID loop to be much more precise in controlling the temperature of the LEDs. The small changes in temperature were easily detected and could be corrected for within the PID loop.

The proportional factor is the most straightforward of the three factors in this control loop. The output of the proportional factor is directly correlated to the gain that is set and the

error which is quantified as the difference between the setpoint and the feedback. As a result, if the proportional gain is set high, the control loop can overshoot the set point often. These continual overshoots can produce oscillations. The proportional factor is important to control the speed of the response of the control system, however if this value is increased in excess the oscillations will be too large and the system will be unstable.

The next response in the PID loop is the integral response. This factor corrects for the accumulation of error. This component is the factor that is responsible for storing the error over time. Positive and negative errors will be able to cancel each other out in this component and as a result when the integral response is acting appropriately it eliminates the steady state offset. At some points this integral response can contribute to the output overshoot past the set point, which would be not ideal. The smaller the integral time the more aggressively the response reacts.

The final component of the PID controller loop, and probably least understood factor, is the derivative response. Often many PID loops do not even have a derivative response and exist as solely PI loops.[10] However, the derivative response plays an important role in correcting the present error versus the error in the previous instance it was measured. Ultimately, the derivative is monitoring the rate of change of the error. The derivative factor is crucial in counteracting the overshoot that can be caused by the proportional response and the integral response. When used properly, a derivative response can allow for more aggressive proportional and integral factors.[9]

When applying this to the temperature control of the LEDs, proportional responses are very important in dealing with large temperature changes, and the other responses work with the proportional response to make the oscillations smaller and temperature of the LED as stable as possible. Along with the new amplifiers, the PID settings were changed on the LEDs. The PID setting are now 7, 10, 2 for the P, I, and D factors respectively. This allows for quick thermal cooler power changes while also not over correcting to small fluctuations. In practice, the LED

temperature control is now within 0.03 °C with the fluctuations in temperature and visually the thermal cooler power output is much smoother, eliminating major oscillations. It is important to note that depending on the LED, some spectral shapes from the LED are more susceptible to improperly regulated temperature. These sensitivities will affect the stability of the BBCES-III signal during measurements.

There were also major connection issues with the green cavity thermocouple with the old thermocouple amplifier board. When switching to the new amplifier board the entire electrical set up was rewired and soldered. This connection issue was fixed upon the revamping of the thermal set up.

3.3 Optical Troubleshooting

Upon first glance, when comparing all three cavities it would seem that they are all equal in their precision. However, in order to retrieve our reflectivity, the known cross sections of N_2 and Helium are compared and using this ratio and our measurements of these gases, the reflectivity of the mirrors can be calculated.[11] In order to check this reflectivity measurement, Ar is sampled and compared to its known cross section as well.[12] An example of this is shown in Figure 3.3. As seen in the bottom of the figure the residuals have a much larger spread in the red cavity than the other two. It was hypothesized that this effect was caused from the little signal in the red cavity because a white LED was being used and filtered as opposed to a red LED. The green and UV cavities have a green, 540 nm, and a UV, 405 nm, LED for their cavities and they had very good precision. As a result, it was determined that a red LED may help our precision issue in the red cavity, so a few types were purchased and were then each individually optimized.

As a background, the white LED is shown in Figure 3.2 to have a spread of 0.90 Mm^{-1} during the standard deviation experiment.[13] Also, the spread of the percent residuals in the

reflectivity were 3.8 %, making this the least precise of the three cavities. The goal of replacing the LED in this cavity is to improve upon this.

The first LED that was attempted was LZ1-10R202-0000 (LED ENGIN) and as shown by Figure 3.4, the initial standard deviation experiment was again run and showed a standard deviation value of 0.48 Mm^{-1}. This is an improvement upon the white standard deviation value of 0.90 Mm^{-1}, which is what the original goal was. With this benchmark met the next step was to validate the use of this LED by taking a reflectivity measurement and then checking the accuracy of this measurement with the Rayleigh scattering by Argon. The result of this run is shown in Figure 3.5. At this point it is apparent that there is a large issue with some of the wavelengths within this red cavity which is made apparent by the large peak in the reflectivity curve, and the peak in the Argon Rayleigh scattering fit. When analyzed, it was noticed that the spectral shape of the LED, shown in Figure 3.6, had a very steep slope over these same wavelengths. This large slope makes small shifts in temperature have a very large impact on the overall intensity and signal of this LED. At this point the new thermocouple amplifiers were installed, and even with this better temperature control the output of these experiments were essentially identical. After optimization of the PID setting for this LED were completed a second reflectivity, Figure 3.7, was measured and this gave better results, but not as consistently as the white LED. The same wavelength region would sometimes be an issue. A potential solution for this was to use a red LED with similar spectral shape but higher power so that there would be more signal for the spectrophotometer to work with.[14]

The next LED that was selected to fix this issue in the red cavity was LZ4-40R208-0000 (LED ENGIN). This high-power LED needed a separate power source than the green and UV cavities, so throughout the experiments the green and UV cavities were not utilized. Upon completing the first standard deviation test, it was clear that this LED had the same issues as the

LZ1, where it was highly temperature dependent in the steep slope region of the spectral shape (Figure 3.8). However, this spectral slope occurred in longer wavelengths than the LZ1, so it was possible to sample outside of this shape if the temperature shift was manipulated to the advantage of the BBCES-III. The next trouble shooting step was to attempt to change the temperature that the PID loop kept the LED at in hopes that this would shift the large slope out of the spectral region that the BBCES-III samples at as shown by Figure 3.9. Temperature points at 90 °C, 80 °C, and 75 °C were chosen as test points for the PID loop. At 75 °C the wavelength region seemed unstable as shown in Figure 3.10. Also, 90 °C seemed to have the same trouble with that spectral region shown in Figure 3.11. However, at 80 °C the standard deviation seemed to be the most ideal, as displayed in Figure 3.12, so at this point the PID loop was optimized for 80 °C. Through this experiment it was shown that there were better standard deviation values than the white LED. At this point the next step was to evaluate the Rayleigh scattering by argon, this showed the same large peak as the LZ1 however it was shifted. This temperature shift was shown to move the problem region farther to the longer wavelengths meaning the wavelength coverage of the BBCES-III would not suffer too much. The standard deviation around the measurement was also substantially improved so it was decided that the LZ4 could be an alternative to the original white LED, as long as the longer wavelengths would not be included. However, it is not ideal to lose wavelengths if it is not necessary. It was discovered that the spectral shape of the LED needed to be different than the LZ1 and LZ4. Due to limited LED options for the red wavelengths, other white LEDs were purchased in hopes that the broader spectral shape would eliminate the temperature dependent trouble region.[15]

The succeeding LED was a high-power white LED, XLamp CXB1816 (CREE) that again required its own power source. This spectral shape, shown in Figure 3.14, is shown to have smooth region over the wavelengths of interest in the red cavity. However, upon operating the

white LED it was found that the temperature that the LED ran at was extremely hot and was not ideal for the thermal coolers to operate. This LED seemed visibly unstable so there was no need for the standard deviation experiment to be run with this high-power white LED. It was at this point that it was proposed to attempt a lower power white LED that just may be more stable than the old white LED.[16]

The new LED, XPLAWT-00-0000-000HU60E8-BS01 (Opulent), when initially installed had a much higher intensity that the previous white LED. It was thought that this was due to the age of the old LED and scratches on the lens of the LED from wear and tear throughout the construction of the BBCES-III. Another reason why this LED is an improvement on the old white LED is that the new temperature control along with the higher intensity of the signal may allow less scatter in the red cavity. Upon performing a standard deviation experiment on this setup, it was found that this white LED was much more stable throughout all of the red wavelengths reported by the BBCES-III. As displayed in Figure 3.15, the scatter of this LED was 0.36 Mm^{-1}, which is the best standard deviation thus far and has allowed for the maximum number of useable wavelengths. Reflectivity calculations with this new white LED are shown in Figure 3.16, where it is seen that the scatter is much improved from the original white LED and there is no problem peak region like when using the red LEDs. This was the chosen LED for this setup of the BBCES-III. It was also shown that as a result of the lower amount of extinction in the red wavelength region for the Rayleigh scattering by Argon that there was more likelihood for the residuals to be a higher percentage.[13]

As shown in the standard deviation plot with the new white LED, the UV cavity was now the weakest of the three cavities. This was also thought to be a result of the age of the UV LED. When replaced with a newer LED, it was shown to have more stability and somewhat higher intensity than previously.[17] After running an Allan variance using this new set up it was

determined that these LEDs were optimized. The LOD achieved from the Allan variance shows that these LEDs are stable enough to sample ambient aerosols, which is the end goal of the BBCES-III. The BBCES-III was then validated with NO_2 in order ensure optimal performance, and as shown by Figure 3.17 the agreement with Burrows et al. was very good.[18-21]

3.4 Conclusions

As a result of multiple changes made to the BBCES-III, vast improvements in the instrument's stability have been made. The temperature control of the LEDs has been optimized by purchasing higher resolution thermocouple amplifiers, optimizing PID settings, and rewiring thermal connections. The intensity is no longer affected from lost thermocouple connections, and the signal from the LEDs are constant. There is also higher intensity in both the red and UV cavities than there was initially, which allows for more accurate readings from the spectrophotometer. The reflectivity measurements that must be taken multiple times per day are now reproducible in one attempt, as opposed to many measurements required before. Also, the scatter in each cavity is greatly minimized as a result of the better temperature control and optimal LEDs for each wavelength region. Overall, the changes increased the measurement precision of the BBCES-III.

Chapter 3 Figures

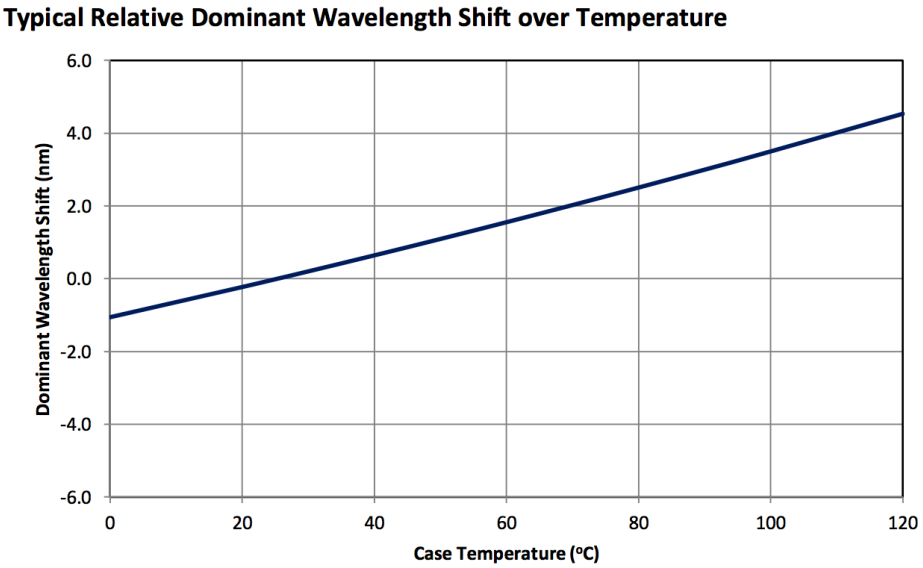

Figure 3.1. Typical Relative Dominant Wavelength Shift over Temperature

The wavelength shift of the green LED, LZ1-00G100, (LED ENGIN), as a function of temperature.[3]

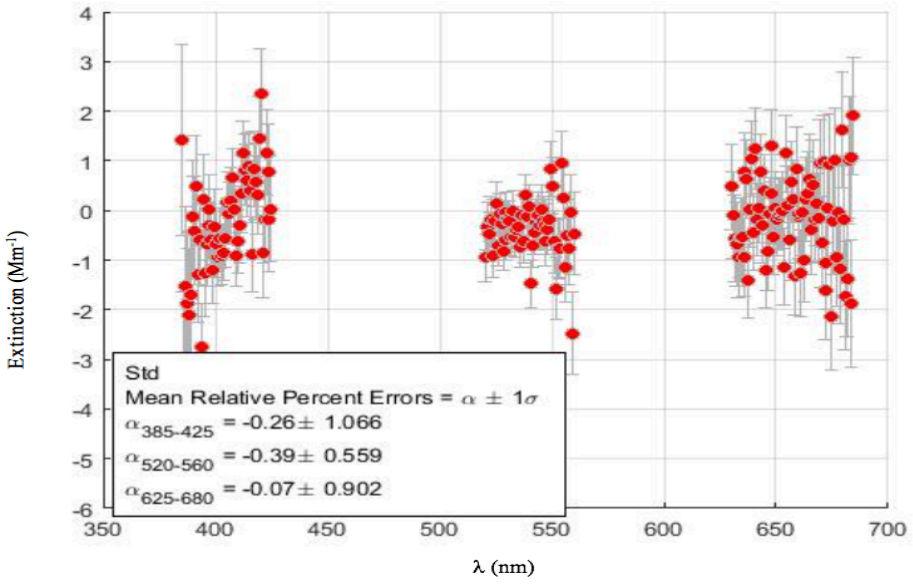

Figure 3.2. Original Standard Deviation Experiment

The standard deviation experiment results for the original BBCES-III set up, using an older white LED, XPLAWT-00-0000-000HU60E8-BS01, (Opulent)

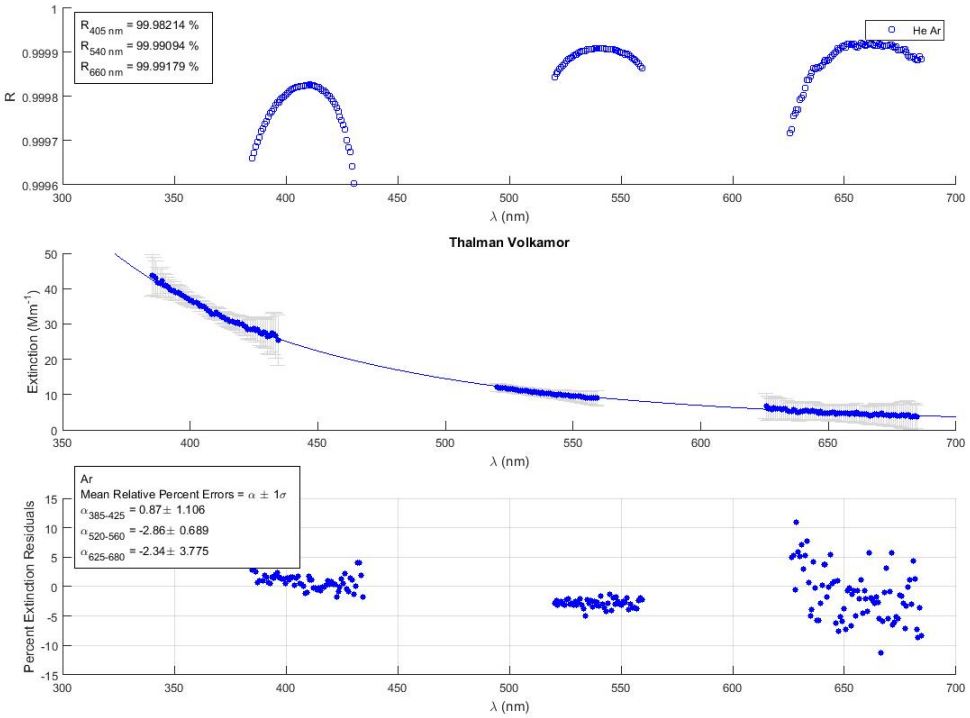

Figure 3.3 Original Reflectivity Experiment and Argon

A typical reflectivity measurement using the original BBCES-III set up. This Reflectivity measurement is then checked using Rayleigh scattering by Argon (middle). Residuals of this Argon check are shown (bottom).

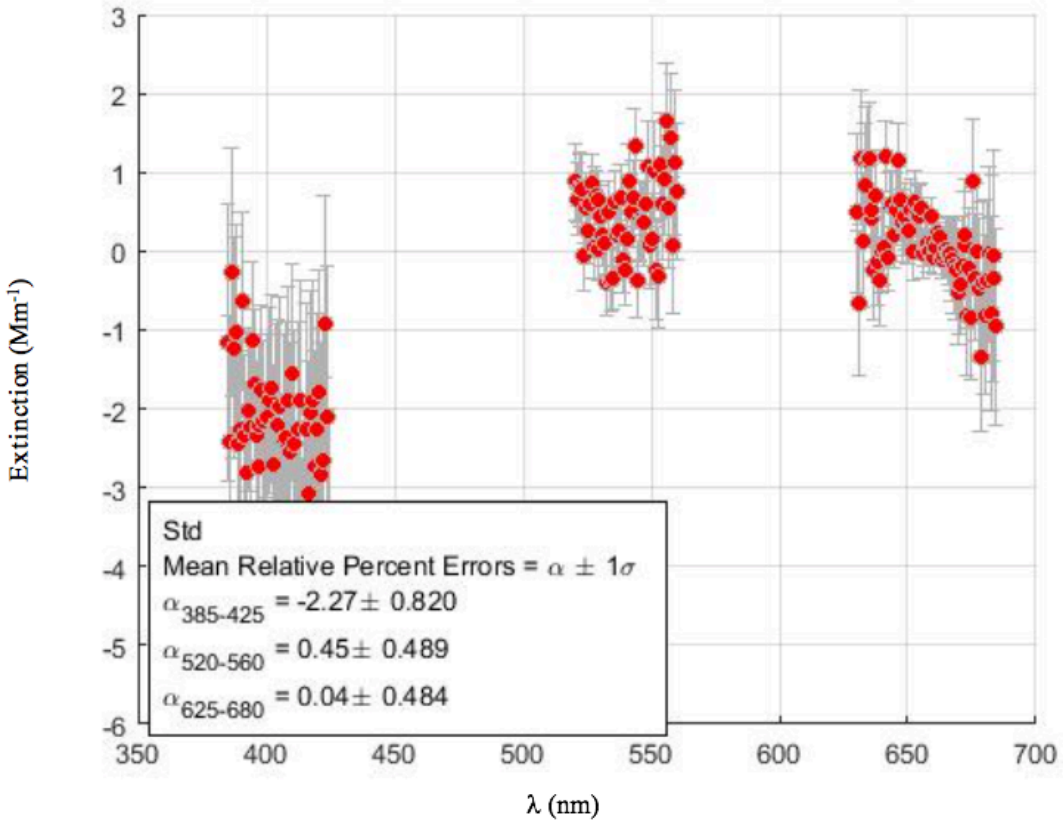

Figure 3.4 LZ1-10R202-0000 Standard Deviation Experiment

The standard deviation experiment results from the original UV and green LEDs and the red LED, LZ1-10R202-0000 (LED ENGIN).

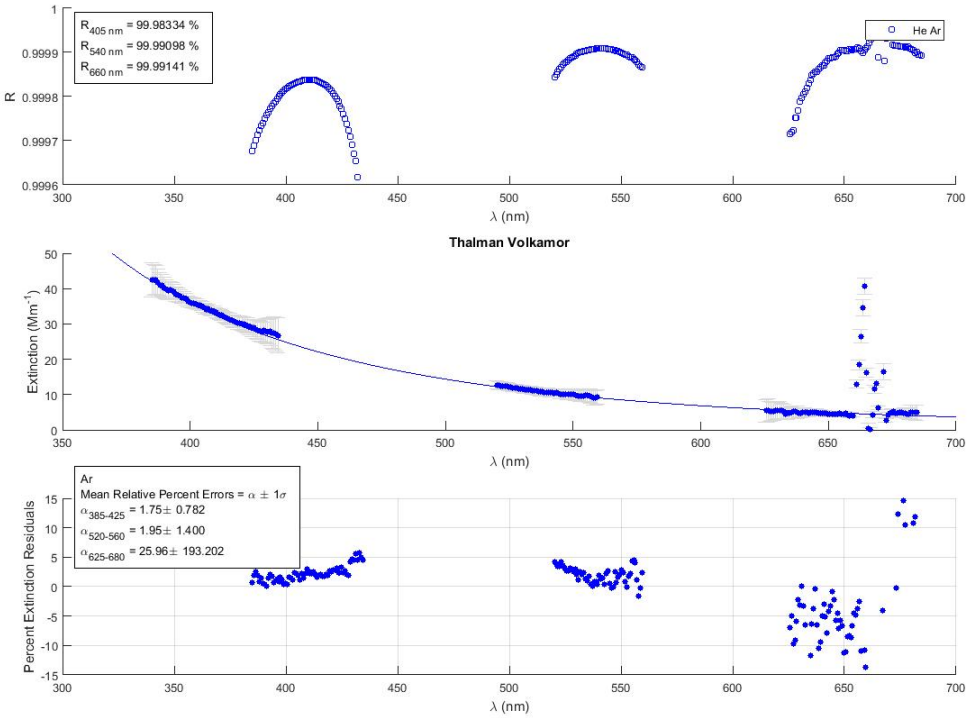

Figure 3.5. LZ1-10R202-0000 Reflectivity Experiment and Argon

The reflectivity results from the red LED, LZ1-10R202-0000 (LED ENGIN), along with Rayleigh scattering extinction by Argon (middle) and residuals from this extinction measurement (bottom).

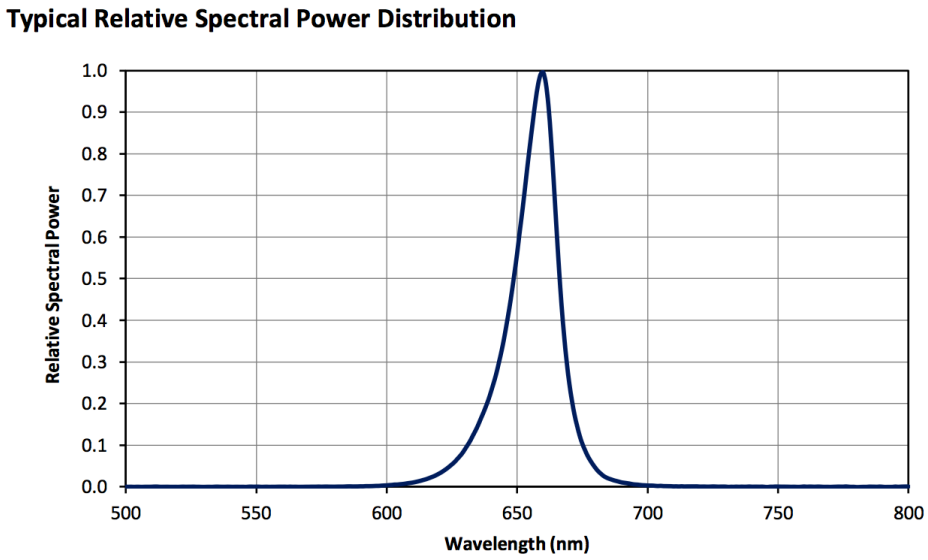

Figure 3.6. Typical Relative Spectral Power Distribution of LZ1-10R202-0000

The spectral power distribution reported for the red LED LZ1-10R202-0000 (LED ENGIN, typically at a temperature of 25 ^{o}C. [14]

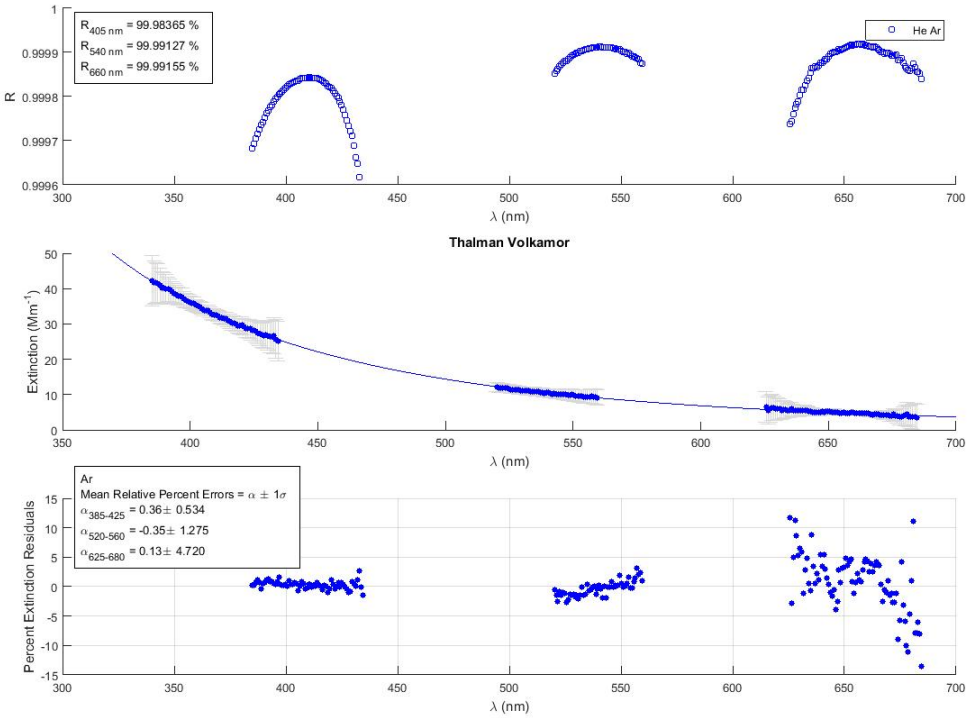

Figure 3.7. Reflectivity and Argon after temperature change of LZ1

The reflectivity results after adjusting the LED temperature from the red LED, LZ1-10R202-0000 (LED ENGIN), along with Rayleigh scattering extinction by Argon (middle) and residuals from this extinction measurement (bottom).

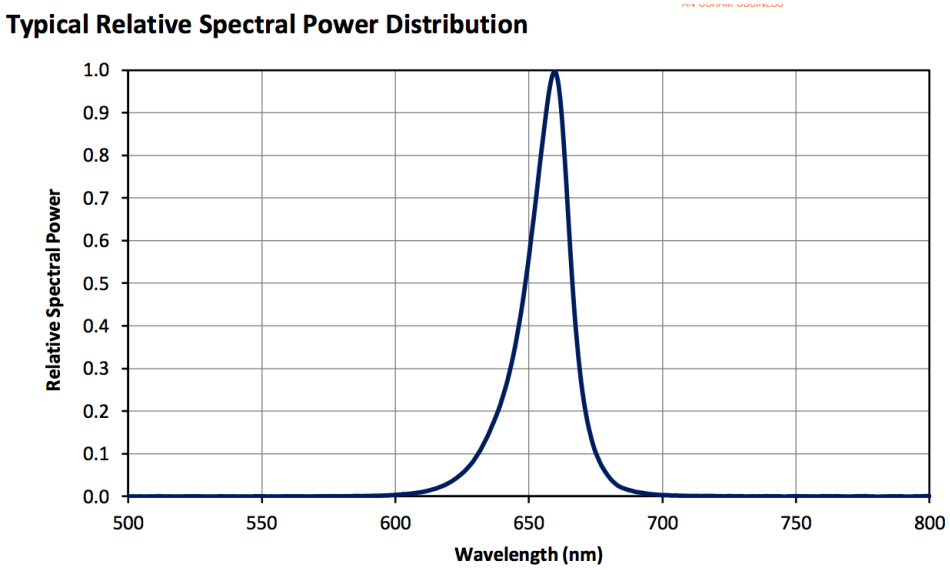

Figure 3.8. Typical Relative Spectral Power Distribution of LZ4-40R208-0000

The relative spectral power distribution of the high-power red LED, LZ4-40R208-0000 (LED ENGIN), at temperature 25 °C.[15]

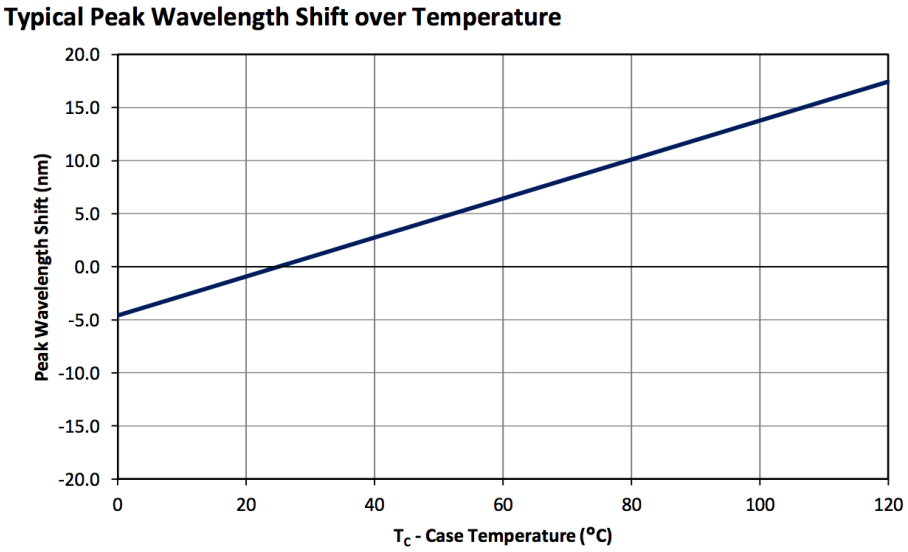

Figure 3.9. Wavelength Shift over Temperature for LZ4-40R208-0000

The wavelength shift of the high-power red LED, LZ4-40R208-0000 (LED ENGIN), as a function of temperature.[15]

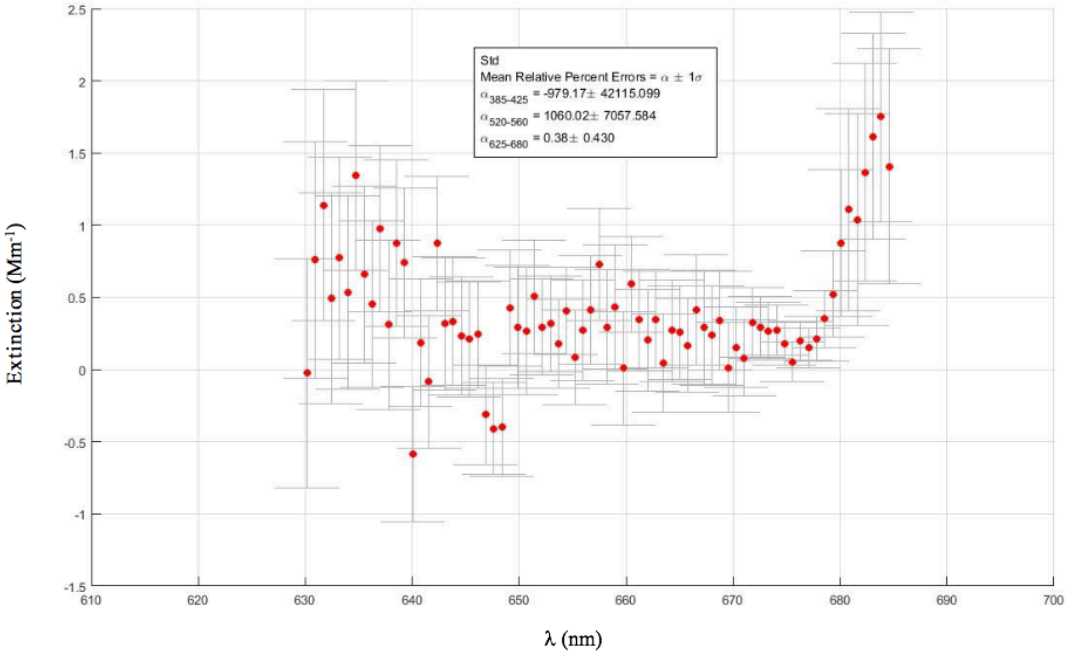

Figure 3.10. LZ4-40R208-0000 Standard Deviation Experiment at 75 ºC

The results of a standard deviation experiment for the high-power red LED LZ4-40R208-0000 (LED ENGIN), when the LED temperature control was set at 75 ºC.

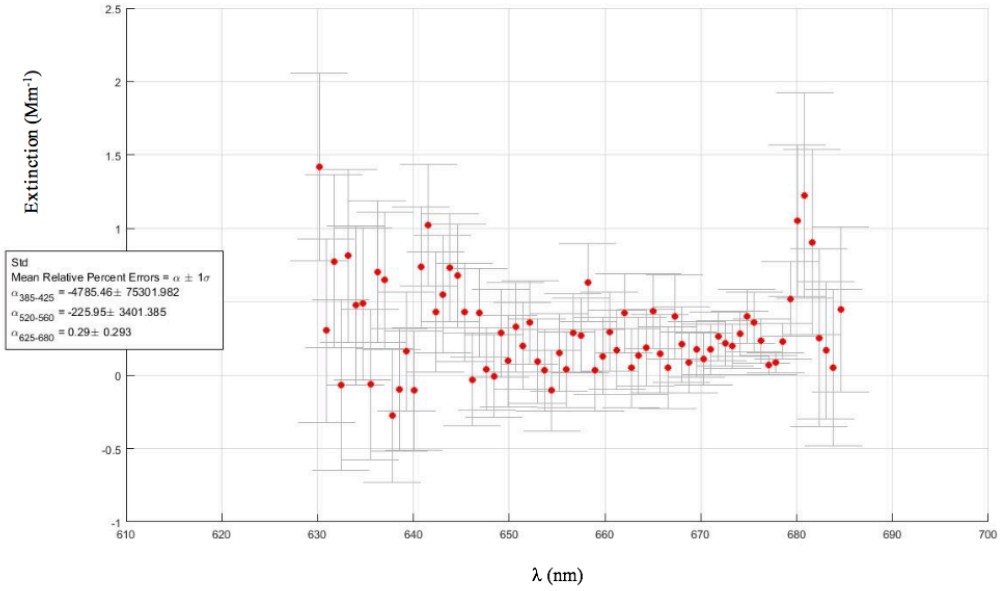

Figure 3.11. LZ4-40R208-0000 Standard Deviation Experiment at 80 ºC

The results of a standard deviation experiment for the high-power red LED LZ4-40R208-0000 (LED ENGIN), when the LED temperature control was set at 80 ºC.

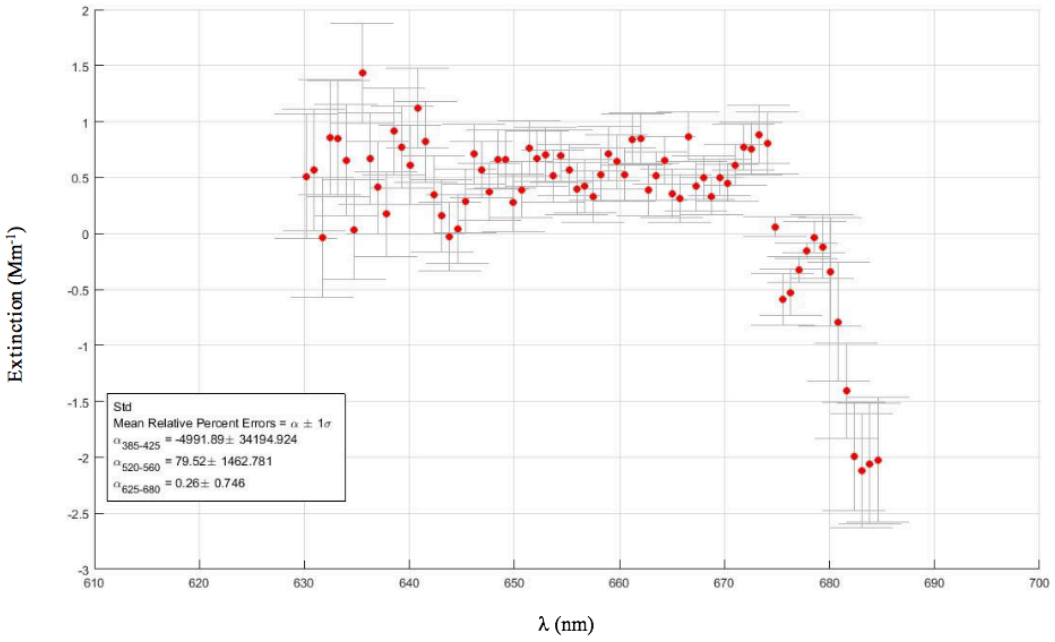

Figure 3.12. LZ4-40R208-0000 Standard Deviation Experiment at 90 ºC

The results of a standard deviation experiment for the high-power red LED LZ4-40R208-0000 (LED ENGIN), when the LED temperature control was set at 90 ºC.

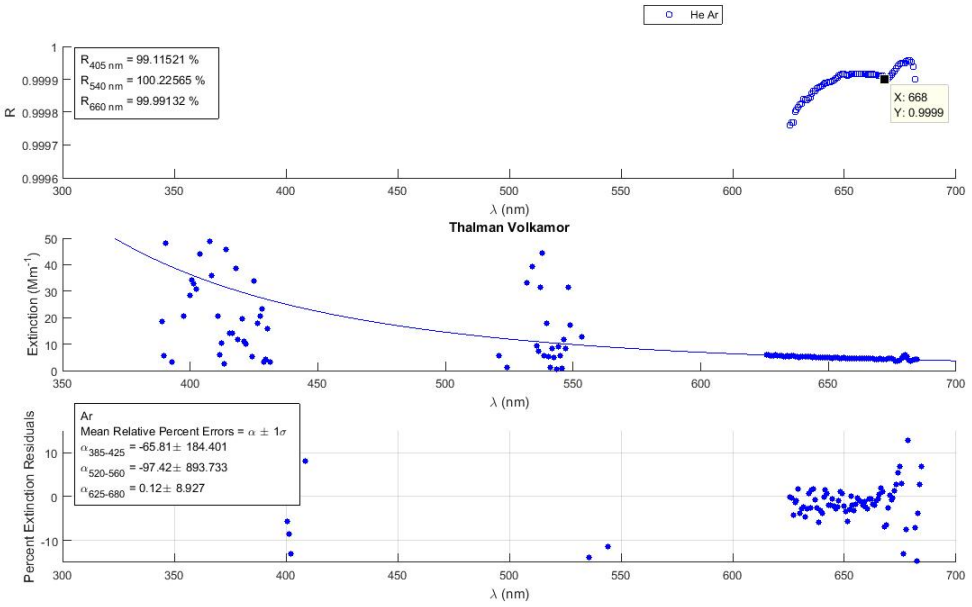

Figure 3.13. LZ4-40R208-0000 Reflectivity Experiment and Argon

The reflectivity results with LED control temperature set at 80 ºC from the high-power red LED, LZ4-40R208-0000 (LED ENGIN). Along with Rayleigh scattering extinction by Argon (middle) and residuals from this extinction measurement (bottom). UV and green cavities were excluded for this experiment.

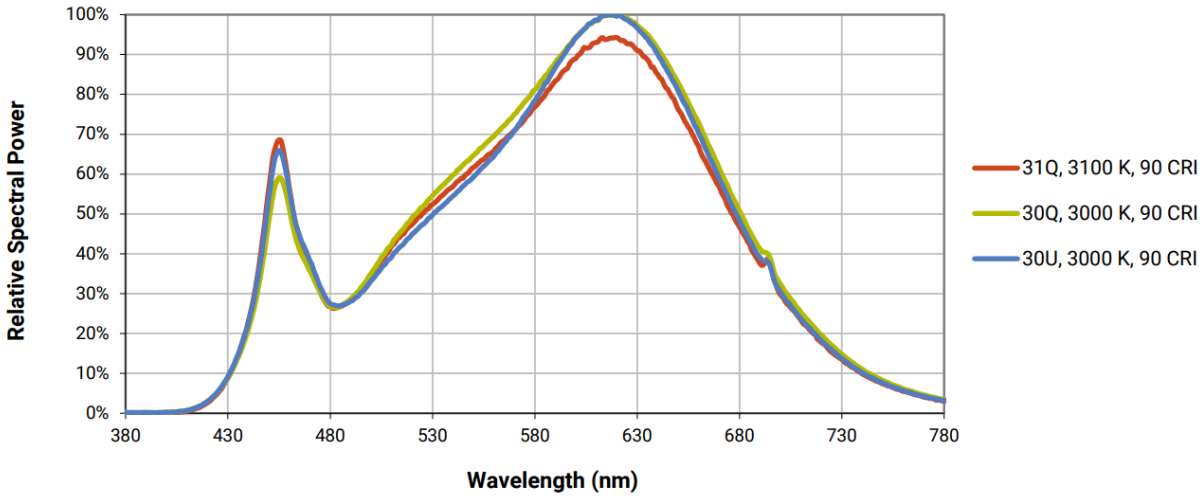

Figure 3.14. Relative Spectral Power Distribution of Cree XLamp CXB1816
The relative spectral power distribution for the high-power white LED, Cree XLamp CXB1816 at a temperature of 85ºC.[16]

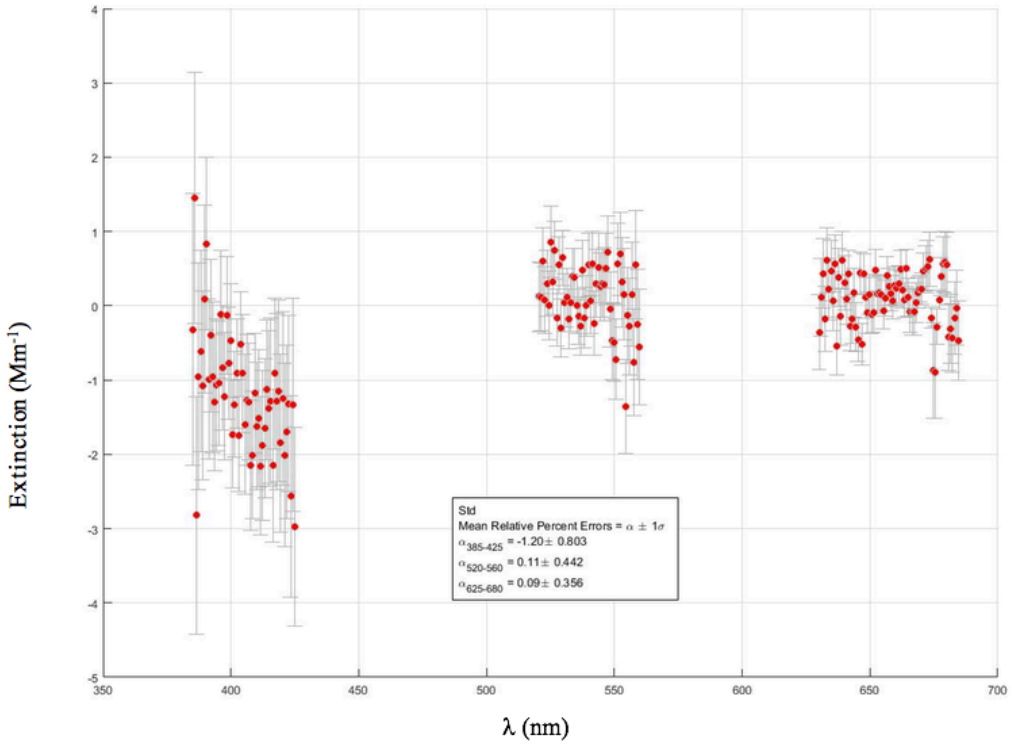

Figure 3.15. XPLAWT-00-0000-000HU60E8-BS01 Standard Deviation Experiment

The standard deviation experiment results for the BBCES-III set up, using the new white LED, XPLAWT-00-0000-000HU60E8-BS01, (Opulent). The green and UV LEDs are from the original setup.

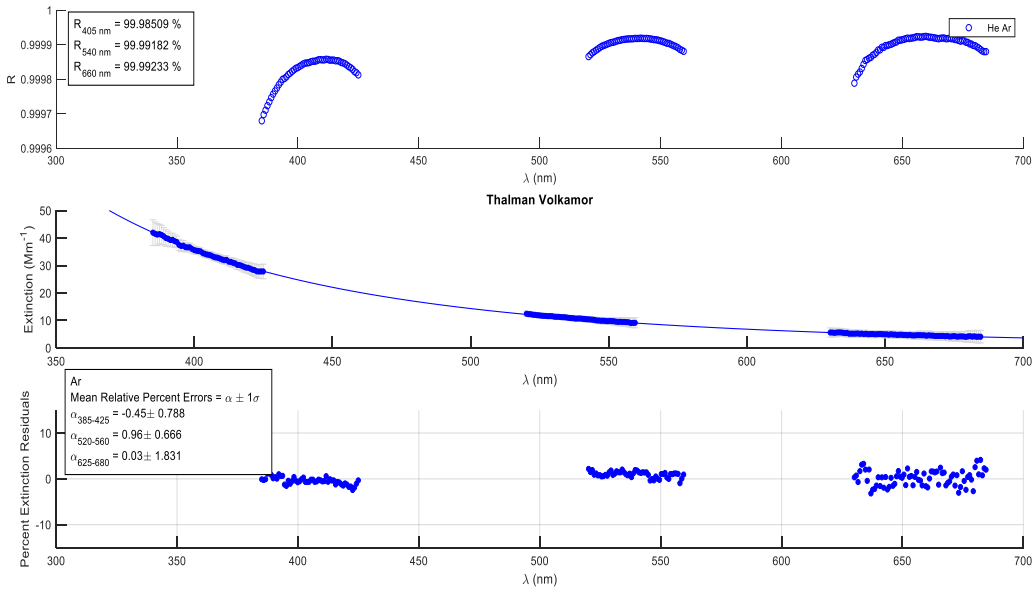

Figure 3.16. XPLAWT-00-0000-000HU60E8-BS01 Reflectivity Experiment and Argon

The reflectivity results from the new white LED, XPLAWT-00-0000-000HU60E8-BS01, (Opulent). Along with Rayleigh scattering extinction by Argon (middle) and residuals from this extinction measurement (bottom).

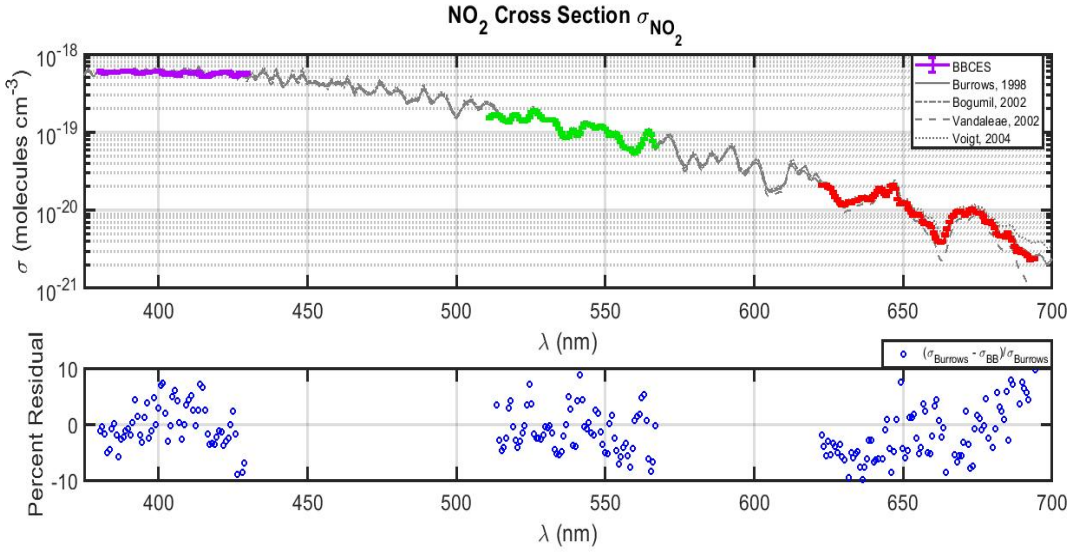

Figure 3.17. NO_2 Measurements with the new LED setup

The NO_2 extinction cross section measured by the new BBCES-III setup (top), with new LEDs in both the red and UV cavities. This measured cross section is superimposed over measurements from Burrows et al., Bogumil et al., Vandaleae et al., and Voigt et al. Residuals shown (bottom) are calculated using the cross section from Burrows et al.[18-21]

References

1. Berden, G.; Engeln, R. *Cavity Ring-down Spectroscopy: Techniques and Applications*; Wiley, 2009.
2. Factors Affecting LED Lightings http://www.heatsinkled.com/Factors-Affecting-LED-Lightings-id506462.html (accessed Oct 2, 2019).
3. *LZ1-00G102*; San Jose, CA, 2018.
4. Cutler, L. S.; Searle, C. L. Some Aspects of the Theorv and Measurement of Frequency Fluctuations in Frequency Standards. *Proc. IEEE* **1966**, *54* (2).
5. Tosini, G.; Ferguson, I.; Tsubota, K. Effects of Blue Light on the Circadian System and Eye Physiology. *Mol. Vis.* **2016**, *22*, 61–72.
6. Harshavardhan Goud, E.; Harshika, A.; Akhil, G.; Charishma, D.; Bhupathi, K.; Kumara Swamy, I. Real Time Based Temperature Control Using Arduino. *Int. J. Innov. Eng. Technol.* https://doi.org/10.21172/ijiet.82.030.
7. Scherz, P. *Practical Electronics for Inventors*; McGraw-Hill, 2000.
8. Ashby, D. *Electrical Engineering 101: Everything You Should Have Learned in School--but Probably Didn't*; Newnes, 2012.
9. *MAX31855 Cold-Junction Compensated Thermocouple-to-Digital Converter General Description*.
10. *MAX31856 Precision Thermocouple to Digital Converter with Linearization*.
11. Langridge, J. M.; Ball, S. M.; Jones, R. L. A Compact Broadband Cavity Enhanced Absorption Spectrometer for Detection of Atmospheric NO2 Using Light Emitting Diodes. *Analyst* **2006**, *131* (8), 916. https://doi.org/10.1039/b605636a.

12. Thalman, R.; Zarzana, K. J.; Tolbert, M. A.; Volkamer, R. Rayleigh Scattering Cross-Section Measurements of Nitrogen, Argon, Oxygen and Air. *J. Quant. Spectrosc. Radiat. Transf.* **2014**, *147*, 171–177. https://doi.org/10.1016/J.JQSRT.2014.05.030.
13. *Opulent-Americas Data Sheet Cree High Power Starboards*; Raleigh, NC, 2019.
14. *High Efficiency Deep Red 660 Nm LED Emitter LZ1-00R202*; San Jose, CA, 2018.
15. *High Radiant Flux Deep Red LED Emitter LZ4-00R208*; San Jose, CA, 2018.
16. *PRODUCT FAMILY DATA SHEET Cree XLamp CXB1816 LED*; 2015.
17. *High Efficiency VIOLET LED Emitter LZ1-00UB00*; San Jose, CA, 2018.
18. K. Bogumil, J. Orphal, T. Homann, S. Voigt, P. Spietz, O.C. Fleischmann, A. Vogel, M. Hartmann, H., Bovensmann, J. Frerick, and J.P. Burrows, "Measurements of molecular absorption spectra with the SCIAMACHY pre-flight model: Instrument characterization and reference data for atmospheric remote sensing in the 230-2380 nm region", J. Photochem. Photobiol. A: Chem. 157, 167-184 (2003); DOI: 10.1016/S1010-6030(03)00062-5
19. J.P. Burrows, A. Dehn, B. Deters, S. Himmelmann, A. Richter, S. Voigt, and J. Orphal, "Atmospheric remote-sensing reference data from GOME: Part 1. Temperature-dependent absorption cross-sections of NO_2 in the 231-794 nm range", J. Quant. Spectrosc. Radiat. Transfer 60, 1025-1031 (1998); DOI: 10.1016/S0022-4073(97)00197-0
20. A.C. Vandaele, C. Hermans, S. Fally, M. Carleer, R. Colin, M.-F. Mérienne, and A. Jenouvrier, "High-resolution Fourier transform measurement of the NO_2 visible and near-infrared absorption cross-section: Temperature and pressure effects", J. Geophys. Res. 107(D18), ACH 3-1 - ACH 3-12 (2002); DOI: 10.1029/2001JD000971

21. S. Voigt, J. Orphal, and J.P. Burrows, "The temperature and pressure dependence of the absorption cross-sections of NO_2 in the 250-800 nm region measured by Fourier-transform spectroscopy", J. Photochem. Photobiol. A: Chem. 149, 1-7 (2002); DOI: 10.1016/S1010-6030(01)00650-5

CHAPTER 4

CROSS SECTION THEORY COMPARISIONS

4.1 Techniques to calculate cross sections

When measuring the extinction by particles with broadband cavity enhanced spectroscopy, knowing the cross sections of the bath gas is crucial. Another important role of correct cross sections of gases is because Rayleigh gas extinction can be used to calculate mirror reflectivity. Here, we present two different methods of calculating the cross sections used for these important equations: one, from Washenfelder et al.[1] where previously measured data was empirically fit using a power law to find the cross section, and the other using refractive index based calculations derived from refractive index data for the target gases, explained in detail in Thalman et al.[2] These methods were both fully applied to BBCES-III data, and it was concluded that the n-based methods yielded the best results for this instrument.

The accuracy of the extinction cross sections of gases are vital to the performance of the BBCES-III. Cross sections are used to calculate reflectivity and also extinction, both of which directly affect data of the BBCES-III. The cross section of the bath gas is taken into account in the equation used to calculated extinction, so that when extinction of aerosols are being measured, the Rayleigh scattering of the bath gas can be excluded. This is imperative when measuring all aerosol particles. This is shown in equation 4.1 as the α_{He} variable where in this scenario Helium is the bath gas and the aerosol being measured is Species X as represented by I_x. In this equation R is the reflectivity as a function of wavelength, d_0 is the distance between mirrors, and I_{He} is the intensity by He.

$$\alpha(\lambda) = \left(\left(\frac{1-R(\lambda)}{d_0}\right)\left(1 - \frac{I_x(\lambda)}{I_{He(\lambda)}}\right) + \alpha_{He}(\lambda)\right)\left(\frac{I_x(\lambda)}{I_{He(\lambda)}}\right) \tag{4.1}$$

Another important aspect of broadband cavity enhanced spectroscopy that requires accurate cross sections is the mirror reflectivity calculations. Rayleigh scattering is used in this calculation because it changes in a well-defined way across UV-Vis wavelengths. When taking a reflectivity measurement, the cavity is flushed with a gas, either N_2 or He. The difference in intensity throughput between these two gas measurements is quantified and used in the reflectivity calculation. The reflectivity of the mirrors in each cavity is a function the ratio of the cross sections between two gases and the difference in intensity throughput. This is exhibited by the equation 4.2 below.

$$R(\lambda) = 1 - d_0 \frac{\left(\frac{I_{N_2}(\lambda)}{I_{He}(\lambda)}\alpha_{Ray}^{N_2}(\lambda)\right) - (\alpha_{Ray}^{He}(\lambda))}{1-(\frac{I_{N_2}(\lambda)}{I_{He}(\lambda)})} \quad (4.2)$$

At this point it is apparent that the theoretical cross sections of gases used play a major role in the performance of the BBCES-III. There are different ways to calculate these cross sections, both of which can give similar results, but even small differences can have large effects when applied to measured extinction data. One of the ways to find the cross sections of these Rayleigh gases is to empirically fit the data that was previously measured and thought to be representative of the true cross section. This usually involves a power law fit to the data that was measured. Another method used to calculate these cross sections is dubbed n-based calculations, and is a method based off of refractive index data that is available. Here we will explore which of these methods work better with BBCES-III measured data.

The first method that will be explored is shown in Washenfelder et al. 2013 where the cross sections needed for the reflectivity calculation were empirically fit to previously collected data. The data for nitrogen was retrieved from Bodhaine et al. in 1999,[3] whereas the He data was fitted from data from Shardanand and Rao in 1977[4]. This is reported as $\sigma_{Rayleigh}$ N_2 = $1.2577\times10^{-15} \times \lambda^{-4.1814}$ cm^2 $particle^{-1}$ as the power law fit to the Bodhaine data, and $\sigma_{Rayleigh}$ He = 1.336 ×

$10^{-17} \times \lambda^{-4.1287}$ cm^2 particle^{-1} as the fit to the Shardanand and Rao data. There were a limited number of wavelengths measured as these measurements were made using cavity ringdown spectroscopy (CRDS), and as a result the interpolation between points can lead to a systematic bias and a significant uncertainty in the cross section. The wavelengths that were measured that Washenfelder used to fit the empirically derived power law were 350- 480 nm, which is a significant range but does not cover as broad a spectrum as the BBCES-III which could potentially affect the accuracy of the cross sections in the wavelength region covered.

The second method is covered by Thalman et al.[2] where CRDS was used to derive an absolute cross section of nitrogen at 532 nm and 405 nm. From here BBCES was used to measure relative Rayleigh scattering cross sections of other gases. The scattering cross sections were calculated using n-based calculations from refractive index data. Equation 4.3 exhibits this n-based calculation to find the scattering cross section. In this equation *v* is the wavenumber.

$$\sigma(v) = \frac{24\pi^3 v^4}{N^2}\left(\frac{n_v^2-1}{n_v^2+2}\right)^2 F_k(v) \tag{4.3}$$

This equation requires refractive index data described by Equation 4.4. The values for both of these equations are described in Table 4.1,[5-9] and are derived from a variety of references. The broadband cavity enhanced spectrometer used by Thalman et al. has wavelength coverage from 350 to 650 nm which is more similar to the wavelength coverage of the BBCES-III.

$$(n-1) \times 10^8 = A + \frac{B}{C-v^2} \tag{4.4}$$

Using both of these methods the cross sections are calculated and compared together in Figure 4.1. As shown in this figure there is a significant difference in the nitrogen cross sections but not visibly as much in the helium cross sections. To make this difference easier to visualize the ratio of Washenfelder cross sections to Thalman cross sections was taken and is shown on the right side of the figure. Here it is evident that there is a difference in these cross sections and the difference is larger in the longer wavelength regions. This apparent difference will not only

affect the reflectivity calculations of the mirrors, but also the exclusion of the bath gas from extinction measurements. Here it was imperative to determine which cross section data is best for the BBCES-III data.

4.2 Determining optimal cross sections for reflectivity calculations

Not only are the cross sections used in Washenfelder et al. different from the Thalman et al. cross sections as shown in Figure 4.1, but the equations to calculate reflectivity are different. The reflectivity calculation used in Washenfelder et al.[10] is shown as equation 4.5 below.

$$R = 1 - [d(\alpha_{N2} - \alpha_{He})\left(\frac{I_{N2}}{I_{He} - I_{N2}}\right)] \tag{4.5}$$

In order to be consistent, it was decided that when applying alternative techniques to the BBCES-III it would be wise to be consistent within the same paper. As a result, the reflectivity was calculated using both the reflectivity equation and the cross sections reported by Washenfelder et al. The reflectivity calculation used the ratio of N_2 and He to come up with the reflectivity curves. This result is shown by Figure 4.2, with specific wavelengths chosen for each cavity to be highlighted. This showed reflectivities of 99.9820, 99.9916, and 99.9922 percent for wavelengths 405, 532, and 660 nm respectively.

The Thalman et al. group used Equation 4.2 above to calculate reflectivity. This reflectivity calculation also used the ratio of N_2 and He to produce the reflectivity curves. The result of this reflectivity calculation is shown in Figure 4.3, with the same three wavelengths chosen in each cavity in order to accurately compare the two methods of calculating. This measurement yielded a result of 99.9816, 99.9915, and 99.9918 percent for wavelengths 405, 532, and 660 nm respectively. This result ended up yielding lower reflectivity measurements than the Washenfelder method, as indicated when both methods are plotted on the same scale in Figure 4.5. Although high reflectivity measurements indicate a better LOD, inaccurate, high

reflectivity measurements will yield inaccurate extinction measurements. As such, we are unable to conclusively say that the higher reflectivity measurement is actually favored over the lower. These reflectivities must be applied to extinction measurements in order to fully grasp which cross section calculation method yields the best results for the measurements of the BBCES-III.

4.3 Determining optimal cross sections for extinction measurements

Extinction equations for both of the methods seemingly looked very different, however after a derivation it was proven that the extinction equations for both Thalman et al.[2] and Washenfelder et al.[1] were mathematically equivalent so which equation that was used for BBCES-III data did not matter. In order to fully compare these two methods, the Rayleigh scattering by argon was measured by the BBCES-III and then plotted with the theoretical Rayleigh scattering by argon reported by Thalman et al. as the cross section was not reported and fit by Washenfelder group. For example, if reflectivity was calculated using the cross sections reported by Washenfelder et al., then the theoretical argon measurement was compared to the argon cross section reported by Thalman et al. As a result, it would be expected for reflectivity from the cross sections of Thalman et al. to have better agreement with matching the extinction by argon, because the argon extinction cross section was calculated also using n-based methods.

As shown in Figure 4.5 the Argon extinction using reflectivity calculated from the method reported in Washenfelder et al. had very large relative errors. The red cavity had over 20 percent relative error for certain wavelengths. This is obviously not ideal for extinction measurements as Rayleigh scattering by Argon should be very consistent and easily quantified. In Figure 4.6, the extinction spectra from Argon is shown when the reflectivity is calculated using the cross sections from Thalman et al. As expected, this showed a vast improvement upon the Washenfelder reflectivity extinction spectrum. All cavities have relative percent errors less

than 20 percent, with most wavelengths only having around 10 percent error. However, this result was expected as the Thalman et al. cross sections should be expected to have better agreement with each other as they came from the same method of calculating cross sections. In order to have a truly impartial experiment, a well quantified extinction cross section must be measured by the BBCES-III and compared to a theoretical extinction cross section from neither Thalman et al. or Washenfelder et al.

It was decided that the absorption cross section of NO_2 had a wide variety of measurements and was very well quantified by other groups not being compared in this study. The NO_2 absorption cross section when plotted with the reflectivity calculated from Washenfelder et al.[1] is shown is Figure 4.7. The agreement with Burrows et al. was the most similar to the BBCES-III data and was used to compute residuals. The agreement for the UV and green cavities were within 10 percent residuals whereas the red cavity was greater than 10 percent. The fact that this effect was the highest in the red cavity indicates that maybe this could be fixed with a change in the cross sections used based on the results from Figure 4.1.

Next, this same NO_2 experimental data was analyzed using the reflectivity calculated from the cross sections from Thalman et al.[2] These results were also compared to Burrows et a. in order to calculate the percent residuals. As shown in Figure 4.8, the agreement was within 10 percent for all reported wavelengths including the red cavity. This is indicative that the cross section method reported by Thalman et al. resulted in better agreement with NO_2 absorption cross sections. The NO_2 absorption cross section has been thoroughly studied, and having good agreement with previous groups suggests that this n-based method is a reasonable one. This also leads us to believe that the reflectivity calculations are more accurate for the BBCES-III using this n-based calculation method.

Chapter 4 Figures

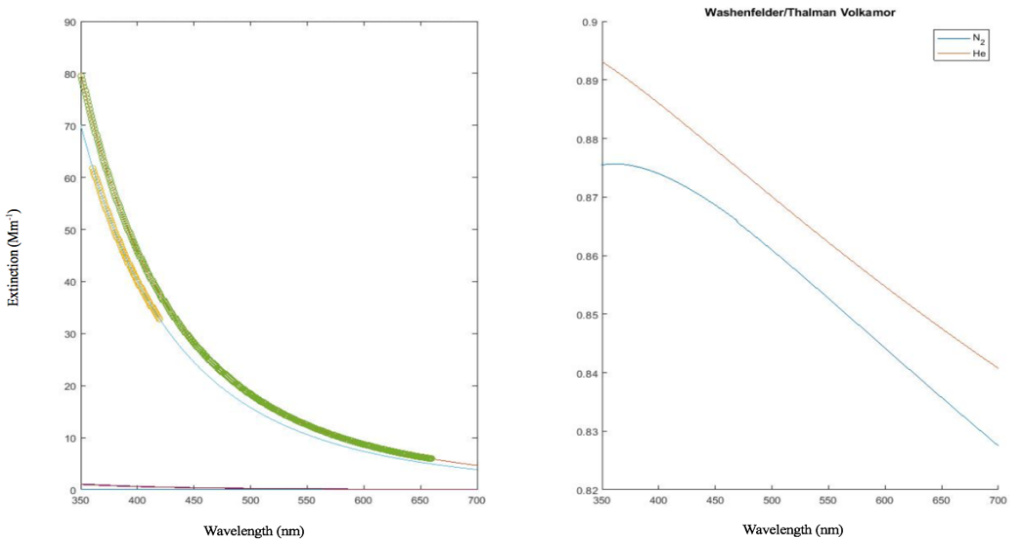

Figure 4.1. Cross Section Comparisons

Left. The reported wavelength dependent cross sections of N_2 by Washenfelder et al. (yellow) and Thalman et al. (Green) with their measured wavelength region highlighted.
Right. The ratio of Washenfelder cross sections to Thalman cross sections for both N_2 (blue) and He (orange).

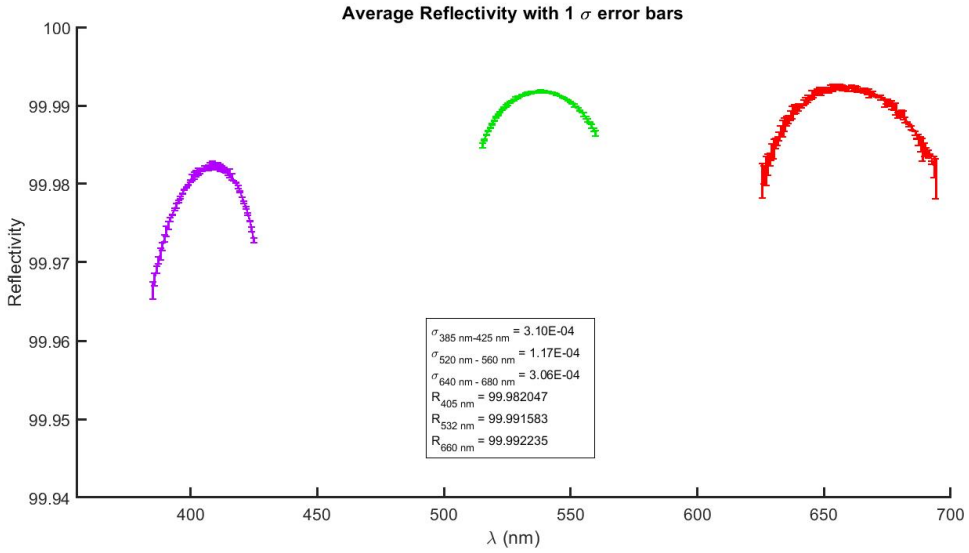

Figure 4.2 Reflectivity using Washenfelder Cross Sections

Reflectivity curves calculated from the measured extinction of He and N_2 and the ratio of the cross sections of these two gases calculated from the empirically derived formula from Washenfelder et al.

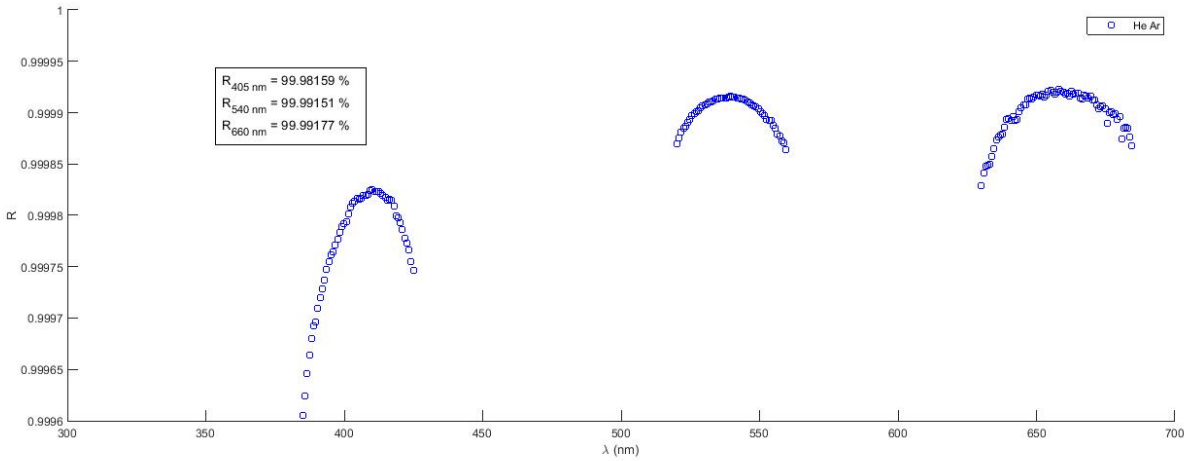

Figure 4.3. Reflectivity using Thalman Cross Sections

Reflectivity curves calculated from the measured extinction of He and N_2 and the ratio of the cross sections of these two gases calculated from the n-based method from Thalman et al.

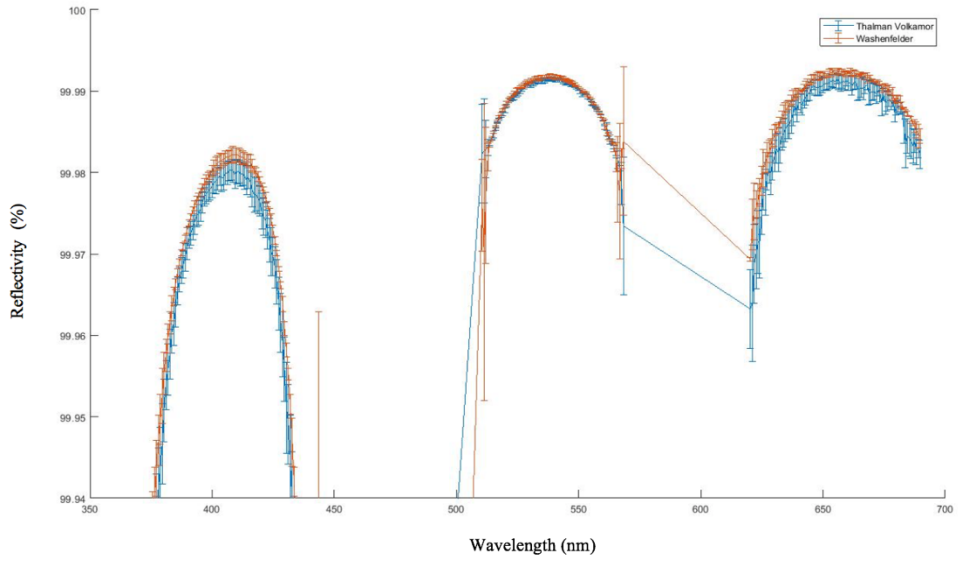

Figure 4.4. Reflectivity Curves using both Methods

Reflectivity curves from both approaches of cross section derivations, plotted with each other. Thalman et al. reflectivity in blue and Washenfelder et al. reflectivity in orange.

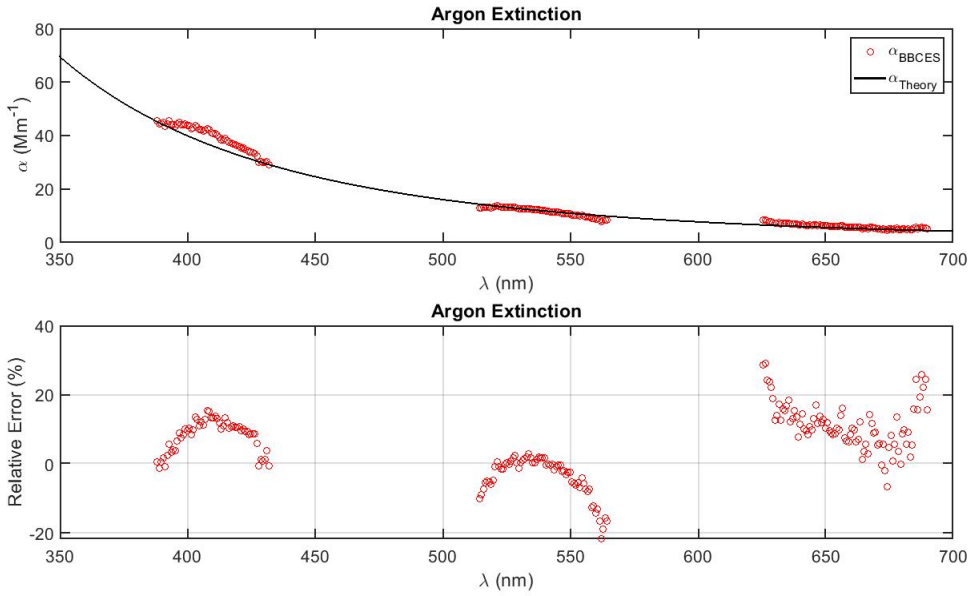

Figure 4.5. Extinction by Argon using Washenfelder et al.

Argon extinction spectra measured by the BBCES-III using the reflectivity calculated from Washenfelder et al. The residuals are compared to the theoretical extinction calculated by Thalman et al.

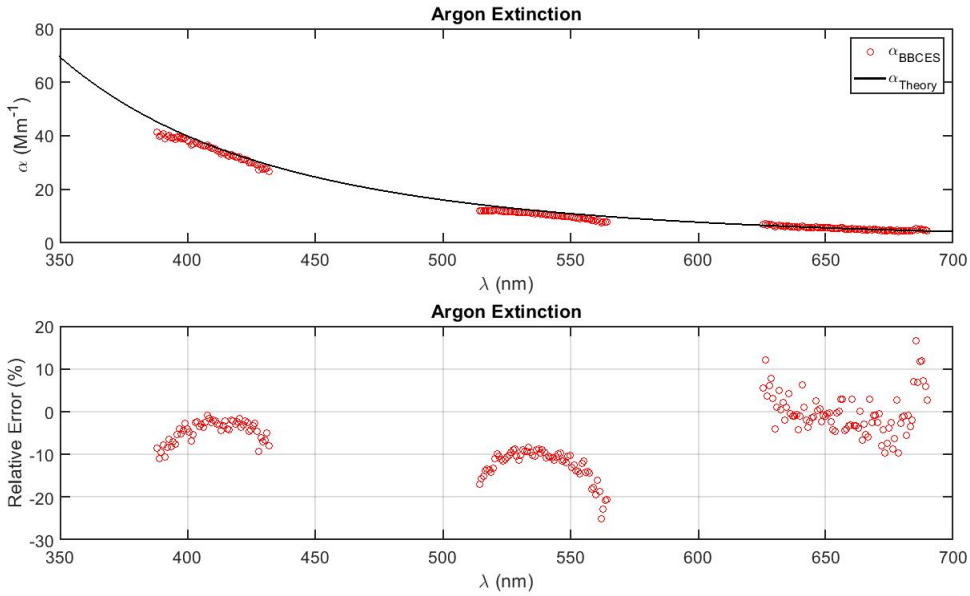

Figure 4.6. Extinction by Argon using Thalman et al.

Argon extinction spectra measured by the BBCES-III using the reflectivity calculated from Thalman et al. The residuals are compared to the theoretical extinction calculated by Thalman et al.

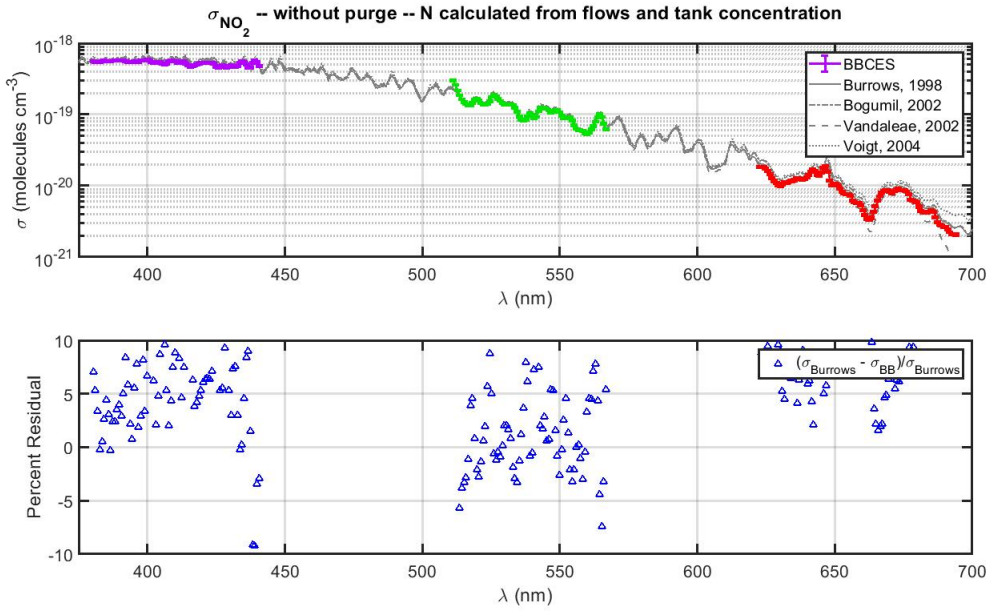

Figure 4.7. NO_2 Measured Absorption Cross Section using Washenfelder et al.

NO_2 absorption cross section measured by the BBCES-III using the reflectivity calculated from Washenfelder et al. The residuals are compared to the theoretical extinction calculated by Thalman et al.

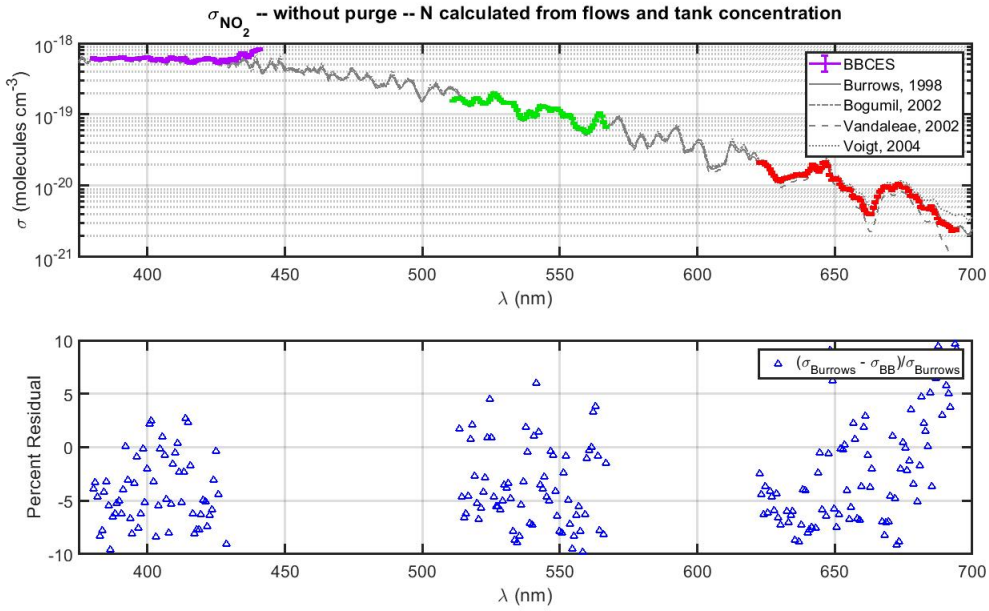

Figure 4.8. NO_2 Measured Absorption Cross Section using Thalman et al.

NO_2 absorption cross section measured by the BBCES-III using the reflectivity calculated from Thalman et al. The residuals are compared to the theoretical extinction calculated by Thalman et al.

Table 4.1 Values need for Refractive Index Calculations

Gas	A	B	C	King Correction Factor (F_k)
$He^{a,b}$	2283	1.8102×10^{13}	1.5342×10^{10}	$F_k(\nu) = 1$
$N_2^{a,c}$	5677.465	318.81874×10^{12}	14.4×10^{9}	$F_k(\nu) = 1.034 + 3.17 \times 10^{-12}\nu^2$
$N_2^{a,d}$	6498.2	307.43305×10^{12}	14.4×10^{9}	$F_k(\nu) = 1.034 + 3.17 \times 10^{-12}\nu^2$
$Ar^{a,e}$	6432.135	286.06021×10^{12}	14.4×10^{9}	$F_k(\nu) = 1$
$O_2^{f,g}$	20564.8	2.480899×10^{13}	4.09×10^{9}	$F_k(\nu) = 1.096 + 1.385 \times 10^{-11}\nu^2 + 1.448 \times 10^{-20}\nu^4$

a. Use $N = 2.546899 \times 10^{19}$ molecules cm^{-3}
b. $14285 < \nu < 33333$ cm^{-1}
c. $21360 < \nu < 39370$ cm^{-1}
d. $4860 < \nu < 21360$ cm^{-1}
e. $5000 < \nu < 33000$ cm^{-1}
f. Use $N = 2.68678 \times 10^{19}$ molecules cm^{-3}
g. $18315 < \nu < 34722$ cm^{-1}

References

1. Washenfelder, R. A.; Flores, J. M.; Brock, C. A.; Brown, S. S.; Rudich, Y. Broadband Measurements of Aerosol Extinction in the Ultraviolet Spectral Region. *Atmos. Meas. Tech* **2013**, *6*, 861–877. https://doi.org/10.5194/amt-6-861-2013.
2. Thalman, R.; Zarzana, K. J.; Tolbert, M. A.; Volkamer, R. Rayleigh Scattering Cross-Section Measurements of Nitrogen, Argon, Oxygen and Air. *J. Quant. Spectrosc. Radiat. Transf.* **2014**, *147*, 171–177. https://doi.org/10.1016/J.JQSRT.2014.05.030.
3. Shardanand; Rao, A. *ABSOLUTE RAYLEIGH SCATTERING CROSS SECTIONS OF GASES A N D FREONS OF STRATOSPHERIC INTEREST I N THE VISIBLE A N D ULTRAVIOLET REGIONS*; 1977.
4. Bodhaine, B. A.; Wood, N. B.; Dutton, E. G.; Slusser, J. R.; Bodhaine, B. A.; Wood, N. B.; Dutton, E. G.; Slusser, J. R. On Rayleigh Optical Depth Calculations. *J. Atmos. Ocean. Technol.* **1999**, *16* (11), 1854–1861
5. Cuthbertson, C.; Cuthbertson, M. The Refraction and Dispersion of Neon and Helium. *Proc. R. Soc. A Math. Phys. Eng. Sci.* **1932**, *135* (826), 40–47. https://doi.org/10.1098/rspa.1932.0019
6. Leonard, P. J. Refractive Indices, Verdet Constants, and Polarizabilities of the Inert Gases. *At. Data Nucl. Data Tables* **1974**, *14* (1), 21–37. https://doi.org/10.1016/S0092-640X(74)80028-8.
7. Bates, D. R. Rayleigh Scattering by Air. *Planet. Space Sci.* **1984**, *32* (6), 785–790. https://doi.org/10.1016/0032-0633(84)90102-8.
8. Sneep, M.; Ubachs, W. Direct Measurement of the Rayleigh Scattering Cross Section in Various Gases. *J. Quant. Spectrosc. Radiat. Transf.* **2005**, *92* (3), 293–310. https://doi.org/10.1016/J.JQSRT.2004.07.025.

9. Berden, G.; Engeln, R. *Cavity Ring-down Spectroscopy : Techniques and Applications*; Wiley, 2009.
10. Washenfelder, R. A.; Langford, A. O.; Fuchs, H.; Brown, S. S. Measurement of Glyoxal Using an Incoherent Broadband Cavity Enhanced Absorption Spectrometer. *Atmos. Chem. Phys.* **2008**, *8* (24), 7779–7793. https://doi.org/10.5194/acp-8-7779-2008.

CHAPTER 5

CONCLUSIONS AND FUTURE DIRECTIONS

Conclusions

The BBCES-III is a valuable instrument for the study of aerosol optical properties, both laboratory-generated and ambient. We have proven that this instrument creates valid extinction measurements and the three cavities have a wide spectral coverage which is ideal for these measurements. Here are presented some future applications for the BBCES-III where the BBCES-III either aids in the characterization of particles or is used to identify ambient aerosol composition. These are useful studies that will have a positive impact on the field of atmospheric chemistry.

5.1 Ammonium Sulfate

The BBCES-III is a three-cavity broadband cavity enhanced spectrometer that has the ability to accurately measure the optical extinction of aerosols even at very low ambient concentrations. The BBCES-III has wavelength coverage from 385-425, 520- 560, and 635-685 nm. This spans the majority of the UV- Visible spectrum, which is key in many climate models. This instrument can measure extinction below 1 Mm^{-1} which is ideal for many applications. The BBCES-III has been validated using a multitude of gases and laboratory generated aerosols. As a result of this validation the results of the BBCES-III can be trusted.

The first future application of the BBCES-III is to better determine the wavelength dependence of the complex refractive index of ammonium sulfate. Ammonium sulfate is a common atmospheric aerosol that is very frequently seen in ambient measurements. Ammonium

sulfate is also commonly measured in laboratory settings and can be used for instrument validation. More importantly, ammonium sulfate is commonly used in climate models to represent purely scattering aerosols, thus the quantification of the complex refractive index is important. In the literature, there is a spread in these refractive index values across the UV-Vis spectrum.[1-9] It is our goal to use BBCES-III data to better quantify the refractive index values of ammonium sulfate.

Experimentally, different particle sizes of ammonium sulfate will be size selected by a DMA and counted by a CPC while being measured by the BBCES-III. The measured extinction cross sections are computed by dividing extinction by the number density. Using a nonlinear least squared optimization algorithm, modelled values that give best agreement with measurements can be determined. The modelled extinction cross section will be computed with Mie theory and will include the refractive index defined by the Sellmeier equation. Additional terms may be added to the model to account for experimental uncertainties. This Sellmeier equation will report the refractive index of ammonium sulfate as a function of wavelength that was retrieved from the BBCES-III measurements. Preliminary data taken for this experiment is proving that this refractive index retrieval should be successful because reasonable refractive indices have been determined and these results will benefit the state of the field.

5.2 Polystyrene Latex Spheres

Polystyrene latex spheres (PSLs) are laboratory generated aerosols that are commonly used to calibrate aerosol optical instruments. Any errors in instrument calibration will directly propagate into the measurements. When any improvement in calibration is done the measurements become more accurate. The next application of the BBCES-III is to retrieve the refractive index of the PSLs to improve these aerosol optical extinction calibrations. Another

aspect of this application is to present a new analytical method to simultaneously derive the refractive index and size distribution. It is planned for this experiment to closely follow the work of Gienger et al.[10] These improvements in the refractive index of PSLs should advance the accuracy of the calibration and hence the measurements of aerosol optical instruments.

Experimentally, the BBCES-III will measure the extinction of PSLs at three different sizes, 600, 800, and 900 nm while the CPC will measure the concentration in parallel with the BBCES-III. The PSLs have a size distribution that is very narrow. Analytically the model used to find the extinction cross section will be similar to the method reported above for ammonium sulfate. This solution shall then be forced to fit a Cauchy equation. There will then be an eleven-parameter fit to this measured data which will simultaneously derive the refractive index, mean particle size, size distribution standard deviation, along with correction factors for particle counting and refractive index errors. The chance of success in this project is high as this application of the BBCES-III is near completion, at the time of this thesis the final adaptation to the retrieval algorithm are being made.

5.3 Aerosol Classification

Another future application of the BBCES-III is still in the preliminary stages. The goal of this application is to show a novel method to optically characterize the types of aerosols by class. The classification of ambient aerosols is important to improve the knowledge of the aerosol composition of the atmosphere. In these measurements, the BBCES-III and the photoacoustic spectrometer are coupled together to retrieve the SSA, AAE, and EAE. Different particles have different EAE, AAE, and SSA. Using chemometric techniques the variation of these properties by each particle type can be distinguished. For example, urban industrial aerosols typically have EAE around 1.8, and a SSA_{440} of 0.97; whereas dust aerosols have an EAE of 0.1 and a SSA_{440}

of 0.9. Using these optical properties to classify aerosols allows for the composition of ambient aerosols to be divided into potential sources.

The absorption of ambient aerosols will be measured by the MultiPAS-IV, while the extinction of these same aerosols will be measured by the BBCES-III. With these optical measurements, chemometric analysis is performed on the ambient data in order to separate and identify different types of aerosols. Some preliminary data has been collected and different chemometric methods are being applied to this data. It is expected that this future direction will have a high chance of success due to agreement of initial measurements to previous classification of aerosols using alternative methods.[11]

References

1. Li, J., Wang, W., Li, K., Zhang, W., Ge, M., & Peng, C. (2019). Development and application of the multi-wavelength cavity ring-down aerosol extinction spectrometer. Journal of Environmental Sciences, 76, 227-237.
2. Xu, X., Zhao, W., Fang, B., Zhou, J., Wang, S., Zhang, W., ... & Chen, W. (2018). Threewavelength cavity-enhanced albedometer for measuring wavelength-dependent optical properties and single-scattering albedo of aerosols. Optics express, 26(25), 33484-33500.
3. Washenfelder, R. A., Flores, J. M., Brock, C. A., Brown, S. S., & Rudich, Y. (2013). Broadband measurements of aerosol extinction in the ultraviolet spectral region. Atmospheric Measurement Techniques, 6(4), 861-877.
4. Toon, Owen B., James B. Pollack, and Bishun N. Khare. "The optical constants of several atmospheric aerosol species: Ammonium sulfate, aluminum oxide, and sodium chloride." Journal of Geophysical research 81.33 (1976): 5733-5748.
5. Michel Flores, J., Bar-Or, R. Z., Bluvshtein, N., Abo-Riziq, A., Kostinski, A., Borrmann, S., ... & Rudich, Y. (2012). Absorbing aerosols at high relative humidity: linking hygroscopic growth to optical properties. Atmospheric Chemistry and Physics, 12(12), 5511-5521.
6. Dinar, E., Riziq, A. A., Spindler, C., Erlick, C., Kiss, G., & Rudich, Y. (2008). The complex refractive index of atmospheric and model humic-like substances (HULIS) retrieved by a cavity ring down aerosol spectrometer (CRD-AS). Faraday discussions, 137, 279-295.

7. Abo Riziq, A., Erlick, C., Dinar, E., & Rudich, Y. (2007). Optical properties of absorbing and nonabsorbing aerosols retrieved by cavity ring down (CRD) spectroscopy. Atmospheric Chemistry and Physics, 7(6), 1523-1536.
8. Pettersson, A., Lovejoy, E. R., Brock, C. A., Brown, S. S., & Ravishankara, A. R. (2004). Measurement of aerosol optical extinction at 532nm with pulsed cavity ring down spectroscopy. Journal of Aerosol Science, 35(8), 995-1011.
9. Lang-Yona, N., Abo-Riziq, A., Erlick, C., Segre, E., Trainic, M., & Rudich, Y. (2010). Interaction of internally mixed aerosols with light. Physical Chemistry Chemical Physics, 12(1), 21-31.
10. Gienger, J., Bär, M., & Neukammer, J. (2018). Extinction spectra of suspensions of microspheres: determination of the spectral refractive index and particle size distribution with nanometer accuracy. *Applied optics*, *57*(2), 344-355.
11. Giles, D. M., Holben, B. N., Eck, T. F., Sinyuk, A., Smirnov, A., Slutsker, I., ... & Schafer, J. S. (2012). An analysis of AERONET aerosol absorption properties and classifications representative of aerosol source regions. *Journal of Geophysical Research: Atmospheres*, *117*(D17).